NASA Contractor Report - CR182179

Computation of the Tip Vortex Flowfield for Advanced Aircraft Propellers

Tommy M. Tsai, Frederik J. de Jong, and Ralph Levy
Scientific Research Associates, Inc.
Glastonbury, Connecticut

August 1988

Prepared for
Lewis Research Center
Under Contract NAS3-24881

National Aeronautics and
Space Administration

SUMMARY

The tip vortex flow field plays a significant role in the performance of a variety of aerodynamic configurations. The flow field in the tip region is complex, three-dimensional, and viscous with large secondary velocities. The large secondary velocities preclude the possibility of using conventional boundary layer solution techniques to compute the tip vortex flow. On the other hand, a solution of the full Navier-Stokes equations that adequately resolves the tip vortex flow field would require formidable computational resources. Therefore, an approximate set of three-dimensional viscous flow equations which is applicable to the tip vortex flow field but which does not require the resources needed for the solution of the full Navier-Stokes equations is sought. The primary/secondary flow equations represent such a set. These equations contain the physics of steady state tip vortex generation and can be solved numerically by an efficient forward marching procedure.

An earlier Phase I effort established the feasibility of computing the tip flow field in advanced aircraft propellers using a forward-marching computation procedure. The effort demonstrated the capability of the forward-marching procedure to compute generation and roll-up of the tip vortex. Further, Phase I results have shown capability in handling complex geometry of advanced propeller blades.

The Phase II effort built on the framework established by the Phase I study for advanced propeller blade tip flow field computations. The objective of the proposed Phase II study was to provide a computer code capable of predicting the tip flow field in advanced aircraft propellers.

The Phase II study accomplished the following tasks:

1. A procedure was developed for inclusion of potential flow chordwise pressure gradients into the aircraft propeller analysis. The pressure field comes from use of the Hess panel code.

2. The grid generation package was generalized from that used in the Phase I program to allow specification of more general blade shapes and to permit specification of grids appropriate for turbulent flow calculations around advanced propeller blades.

3. The generation of a tip vortex on the SR3 advanced aircraft propeller was calculated at a Reynolds number of 1.1×10^6 and included high subsonic Mach numbers of approximately 0.8 near the propeller tip. A series of both laminar and turbulent flow cases were run showing the tip vortex generation process on the SR3 blade.

4. The forward marching procedure was extended to compute flow aft of an unswept blade trailing edge.

5. A parametric study was performed to determine the effect of tip thickness on vortex intensity. The blade thickness was varied from 2% of tip chord to 12% of tip chord.

6. Flow field computations from the forward marching procedure were compared with F4 experimental data provided by NASA. Since most of the data was downstream of the blade, the data comparison could only be qualitative.

A Users Manual was prepared.

INTRODUCTION

The tip vortex flow field plays a significant role in the performance of a variety of aerodynamic configurations. Typical examples can be found associated with advanced aircraft propellers, the wing tip of fixed wing aircraft, and the helicopter rotor blade. When any of these configurations produce a force normal to its mean chord line, the flow field is characterized by the surface pressure on one side exceeding that on the other, thus producing lift and drag. This unequal pressure distribution must be gradually relieved in the vicinity of the tip, since at the tip no pressure differential is possible. Thus, at any given chord station the flow field in the tip region is characterized by a high pressure surface (the pressure surface) on which the pressure normally decreases as the tip is approached and a low pressure surface (the suction surface) on which the pressure normally increases as the tip is approached; at the tip location itself the two pressures become equal. This general pressure field leads to a secondary flow outward on the pressure surface, around the tip, and inward on the suction surface. The secondary flow field generated leads to the development of the tip vortex. The tip vortex may play a significant role in the drag and noise characteristics of the configuration. A method of better understanding these phenomena and helping the design engineer avoid related problems would be a valuable asset to the aerodynamic community.

The flow field in the tip region is complex, three-dimensional, and viscous with large secondary velocities. The large secondary velocities preclude the possibility of using conventional boundary layer solution techniques to compute the tip vortex flow. On the other hand, a solution of the full Navier-Stokes equations that adequately resolves the tip vortex flow field would require formidable computational resources. Therefore, an approximate set of three-dimensional viscous flow equations which is applicable to the tip vortex flow field but which does not require the resources needed for the solution of the full Navier-Stokes equations is sought. The parabolized Navier-Stokes equations represent such a set. These equations contain all the physical processes of steady state tip vortex generation and can be solved economically by a forward marching procedure.

The Phase I program proposed a demonstration computation to show feasibility of computing high subsonic, high Reynolds number flow in the blade tip region of advanced aircraft propellers. A simple blade tip geometry was proposed for the

demonstration computation. This objective of the Phase I program has been successfully accomplished.

The Phase II program extends the Phase I study to provide routine analysis of the propeller tip vortex generation process for high Reynolds number flows and advanced aircraft propeller blades. The resulting computer code is designated PEPSIG/SR3.

MAIN TEXT

OVERVIEW

The Phase I effort has established the feasibility of computing the tip flow field in advanced aircraft propellers using a forward-marching computation procedure. The effort has demonstrated the capability of the forward-marching procedure to compute generation and roll-up of the tip vortex. Further, Phase I results have demonstrated the capability for handling complex geometries, such as advanced propeller blades.

The thrust of the Phase II effort is to build on the framework established by the Phase I study for advanced propeller blade tip flow field computations. The objective of the proposed Phase II study is to provide a computer code capable of predicting the tip flow field for advanced aircraft propellers. Such a computer code will be a valuable tool in the design of advanced propeller blades and the analysis of propeller performance. In particular, such a code will be valuable in computing the effects of details of propeller tip geometry on tip vortex generation and suppression.

The Phase II study accomplished the following tasks:

1. A procedure was developed for inclusion of streamwise pressure gradients into the aircraft propeller analysis. The procedure uses the Hess panel method and an interface routine written to interpolate the inviscid pressure gradients onto the viscous grid. Sample calculations using this procedure are presented.

2. The grid generation package was generalized from that used in the Phase I program to allow specification of more general blade shapes and to

permit specification grids appropriate for turbulent flow calculations around advanced propeller blades.

3. The generation of a tip vortex on the SR3 advanced aircraft propeller was calculated at a Reynolds number of 1.1×10^6 and included high subsonic Mach numbers of approximately 0.8. A series of both laminar and turbulent flow cases were run showing the tip vortex generation process on the SR3 blade.

4. The forward marching procedure was extended to compute flow aft of a blade trailing edge. This was demonstrated for a NACA-0012 shaped blade at 6° angle of attack and Reynolds number based on propeller diameter of approximately 10^6. This calculation was used successfully to compute the flow over the blade tip and downstream of the trailing edge including the tip vortex. An attempt was made to extend this technique to blades with swept trailing edges. This extension was unsuccessful and further development is required for these cases.

5. A parametric study was performed to determine the effect of tip thickness on vortex intensity. The blade thickness was varied from 2% of tip chord to 12% of tip chord.

6. Flow field computations from the forward marching procedure were compared with F4 experimental data provided by NASA. Since most of the data was downstream of the blade, the data comparisons could only be qualitative.

7. A Users Manual was prepared.

An overview of the forward-marching computation procedure developed at SRA is first presented. Specific tasks that define the Phase II effort are then identified and discussed in detail.

ANALYSIS

The Phase II effort is based upon solution of a set of three-dimensional, viscous flow, forward-marching equations. The forward marching computation procedure used for the solution of the parabolic Navier-Stokes equations provides an economical and accurate method for computing many three-dimensional viscous flow fields. This procedure, initially developed for internal flow fields (Refs. 1-3), has been extended to the computation of the propeller tip flow field. The governing equations and computational scheme are presented in this section. This procedure is capable of considering both fixed and rotating coordinate systems. The rotational terms in the governing equations can be included in the analysis if the inviscid pressure field includes the effects of rotation. The version of the Hess code available for this study did not include rotation so the calculations presented are for non-rotating cases only.

The governing equations are derived through approximations made relative to a coordinate system fitted to and aligned with the flow geometry under consideration. To address complex geometries, a smooth reference line is identified which represents the primary flow directions and thus links the geometry with the flow approximations. An orthogonal reference line coordinate system is then derived (Ref. 3) which fits the reference line and its normal planes and which remains orthogonal even when the reference line has nonzero torsion. The flow approximations are made in this orthogonal reference line coordinate system and the governing equations are then transformed to a body fitted coordinate system and solved numerically. Transverse coordinate surfaces must be approximately perpendicular to solid walls or bounding surfaces, since diffusion is permitted only in these transverse coordinate surfaces.

Equations governing primary flow velocity, U_p, and a secondary vorticity, Ω_n, normal to transverse coordinate surfaces are derived utilizing approximations which permit solution of the equations as a spatial initial-value problem, provided reversal of the composite streamwise velocity does not occur. Terms representing diffusion normal to transverse coordinate surfaces (in the streamwise direction) are neglected. Secondary flow velocities are determined from scalar and vector surface potential calculations in transverse coordinate surfaces, once the primary velocity and secondary vorticity are known.

Primary-Secondary Velocity Decomposition

In what follows, vectors are denoted by an overbar, and unit vectors by a caret. The analysis is based on decomposition of the overall velocity vector field, $\bar{U}$, into a primary flow velocity, $\bar{U}_p$, and a secondary flow velocity, $\bar{U}_s$. The overall or composite velocity is determined from the superposition

$$\bar{U} = \bar{U}_p + \bar{U}_s \tag{1}$$

The primary flow velocity is represented as

$$\bar{U}_p = U_p \hat{i}_p \tag{2}$$

where $\hat{i}_p$ is a known inviscid primary flow direction determined, for example, from an a priori potential flow solution for the geometry under consideration. A streamwise coordinate direction from a body fitted coordinate system could be used as an approximation to this potential flow direction. The primary velocity, $\bar{U}_p$, is determined from a solution of a primary flow momentum equation. The secondary flow velocity, $\bar{U}_s$, is derived from scalar and vector surface potentials denoted ϕ and ψ, respectively. If $\hat{i}_n$ denotes the unit vector normal to transverse coordinate surfaces, if ρ is density, and if ρ_o is an arbitrary constant reference density, then $\bar{U}_s$ is defined by

$$\bar{U}_s = \nabla_s \phi + (\rho_o/\rho) \nabla \times \hat{i}_n \psi + \bar{v}_i \tag{3}$$

where $\bar{v}_i$ is an imposed velocity vector in the transverse coordinate surface usually obtained from an inviscid flow about the blade and ∇_s is the surface gradient operator defined by

$$\nabla_s = \nabla - \hat{i}_n (\hat{i}_n \cdot \nabla) \tag{4}$$

It follows that since $\hat{i}_n \cdot \bar{U}_s = 0$, then $\bar{U}_s$ lies entirely within transverse coordinate surfaces. Equation (3) is a general form permitting both rotational and irrotational secondary flows and will lead to governing equations which may be solved as an initial-boundary value problem. The overall velocity decomposition

(1) can be written

$$\bar{U} = U_p \hat{i}_p + \nabla_s \phi + (\rho_o/\rho)\nabla x \hat{i}_n \psi + \bar{v}_i \tag{5}$$

Surface Potential Equations

Equations relating ϕ and ψ with U_p, ρ, and the secondary vorticity component, Ω_n, can be derived using Eq. (5) as follows: From continuity,

$$\nabla \cdot \rho \bar{U} = 0 = \nabla \cdot \rho U_p \hat{i}_p + \nabla \cdot \rho \nabla_s \phi + \rho_o \nabla \cdot \nabla x \hat{i}_n \psi + \nabla \cdot \rho \bar{v}_i \tag{6}$$

and from the definition of the vorticity, Ω_n, based on the secondary flow within the transverse surfaces

$$\hat{i}_n \cdot \nabla x \bar{U} = \Omega_n = \hat{i}_n \cdot \nabla x U_p \hat{i}_p + \hat{i}_n \cdot \nabla x (\rho_o/\rho)\nabla x \hat{i}_n \psi + \hat{i}_n \cdot \nabla x \nabla_s \phi + \hat{i}_n \cdot \nabla x \bar{v}_i \tag{7}$$

Since the second to last term in each of Eqs. (6) and (7) is zero by vector identity, Eqs. (6) and (7) can be written as

$$\nabla \cdot \rho \nabla_s \phi = -\nabla \cdot \rho U_p \hat{i}_p - \nabla \cdot \rho \bar{v}_i \tag{8}$$

$$\hat{i}_n \cdot \nabla x (\rho_o/\rho)\nabla x \hat{i}_n \psi = \Omega_n - \hat{i}_n \cdot \nabla x \bar{v}_i - \hat{i}_n \cdot \nabla x U_p \hat{i}_p \tag{9}$$

Note that the last term in Eq. (9) is identically zero in a coordinate system for which $\hat{i}_n$ and $\hat{i}_p$ have the same direction, and would be small if $\hat{i}_n$ and $\hat{i}_p$ are approximately aligned. In any event, given a knowledge of U_p, Ω_n and ρ, the surface potentials ϕ and ψ can be determined by a two-dimensional elliptic calculation in transverse coordinate surfaces at each streamwise location. In turn, $\bar{U}_s$ can be computed from Eq. (3), and the composite velocity $\bar{U}$ will satisfy continuity. Equations for U_p and Ω_n are obtained from the equations governing momentum and vorticity, respectively.

The streamwise momentum equation is given by

$$\hat{i}_p \cdot \left[\left[\bar{U} \cdot \nabla \right] \bar{U} + \left[\nabla P \right] / \rho \right] = \hat{i}_p \cdot \bar{F} + \hat{i}_p \cdot \bar{R} \tag{10}$$

where P is pressure and $\rho \bar{F}$ is force due to viscous stress and terms in $\bar{F}$ representing streamwise diffusion are neglected. ρR is the additional force due

to a rotating coordinate system; where $\bar{R} = -2\bar{\omega}\times\bar{U} - \bar{\omega}\times(\bar{\omega}\times\bar{r})$, and ω is the angular velocity of the coordinate system and $\bar{r}$ is the radius vector from the rotation axis. The pressure term in the streamwise momentum Eq. (10) can be taken from a simpler analysis such as an inviscid flow analysis. While this results in a set of equations which can be solved by forward marching, the surface pressures which are due to the pressure field imposed upon the flow are the inviscid flow pressures. Since the actual surface pressures are often of primary interest, a new estimate of the actual surface pressure which includes viscous and secondary flow effects can be computed from the resulting velocity field in the following manner.

The momentum equations in the transverse surfaces are:

$$\hat{i}_1 \cdot \left[\left(\rho\bar{U}\cdot\nabla\right)\bar{U} + \nabla P - \rho\bar{F} - \rho\bar{R}\right] = 0$$

$$\hat{i}_2 \cdot \left[\left(\rho\bar{U}\cdot\nabla\right)\bar{U} + \nabla P - \rho\bar{F} - \rho\bar{R}\right] = 0 \qquad (11)$$

Equation (11) represents components of the momentum vector in the transverse surfaces:

$$\hat{i}_1\left\{\hat{i}_1 \cdot \left[\left(\rho\bar{U}\cdot\nabla\right)\bar{U} + \nabla P - \rho\bar{F} - \rho\bar{R}\right]\right\} = 0$$

$$\hat{i}_2\left\{\hat{i}_2 \cdot \left[\left(\rho\bar{U}\cdot\nabla\right)\bar{U} + \nabla P - \rho\bar{F} - \rho\bar{R}\right]\right\} = 0 \qquad (12)$$

The divergence of this vector can be written as a Poisson equation for the pressure P at each transverse surface:

$$\nabla_s^2 P = \nabla_s^2\left[P_I + P_c\right] = -\frac{\partial}{\partial x_1}\left\{\hat{i}_1\cdot\left[\left(\rho\bar{U}\cdot\nabla\right)\bar{U} - \rho\bar{F} - \rho\bar{R}\right]\right\}$$

$$-\frac{\partial}{\partial x_2}\left\{\hat{i}_2\cdot\left[\left(\rho\bar{U}\cdot\nabla\right)\bar{U} - \rho\bar{F} - \rho\bar{R}\right]\right\} \qquad (13)$$

where P_I is the imposed pressure, P_c is a viscous correction to the pressure field and x_1 and x_2 are coordinates in the $\hat{i}_1$ and $\hat{i}_2$ directions, respectively. Equation (13) can be solved for the pressure correction, P_c, at each computational station

using Neuman boundary conditions derived from Eq. (12). The use of Neuman boundary conditions requires an additional parameter which is only a function of the normal direction, $P_v(x_3)$, in order to set the level of the pressure field. For external flows, $P_v(x_3)$ is set to match the imposed pressure at an appropriate far field location.

Secondary Vorticity

The equation governing Ω is obtained by cross differentiating each of the transverse momentum equations (11). Eliminating the pressure in the two equations results in a single equation for the transport of the vorticity normal to the transverse surface. This equation has the form

$$\overline{U}\cdot\nabla\Omega_n - \overline{\Omega}\cdot\nabla U_n = G_n + C \tag{14}$$

where G_n is the normal component of the stress terms

$$\overline{G} = \nabla\times\overline{F} \tag{15}$$

and C is a collection of curvature terms arising from changes in orientation of the transverse surface as a function of streamwise coordinate.

Compressibility Relations

The foregoing analysis can be applied to incompressible flows simply be setting $\rho = \rho_o$. Compressibility effects are represented by introducing the perfect gas equation of state $p = \rho RT$ in the imposition of streamwise pressure gradients. For moderate subsonic Mach numbers, inviscid pressure gradients can be obtained either from a compressible potential flow calculation or from an incompressible potential flow corrected for compressibility using, for example, the Prandtl-Glauert formula. From the state equation and the temperature-enthalpy relation

$$E = c_p T + \frac{\overline{U}\cdot\overline{U}}{2} \tag{16}$$

where c_p denotes specific heat. The following auxiliary equation relating the imposed pressure gradients with density, velocity, and total enthalpy is obtained:

$$\hat{i}_p \cdot \nabla \left[P \right] = \hat{i}_p \cdot \nabla \left[\frac{\gamma - 1}{\gamma} \rho \left(E - \frac{\bar{U} \cdot \bar{U}}{2} \right) \right] \tag{17}$$

where γ is specific heat ratio and E is total enthalpy.

In many problems of interest, it can be assumed that the total enthalpy is a constant E_o. This assumption is reasonable for inviscid flow regions with no heat addition and for boundary layers on adiabatic walls provided the Prandtl number is unity. To make this assumption, E is replaced by E_o in Eq. (17), and it is then unnecessary to solve the energy equation, even though the flow is compressible.

Turbulence Model

For tip vortex flow calculation, mixing length models were used in the region upstream of the trailing edge. An isotropic eddy-viscosity formulation was used for the Reynolds stresses:

$$\rho \overline{V_j' \; V_j'} = - \frac{\mu_T}{Re} \frac{\partial V_j}{\partial X_i} \tag{18}$$

The effective turbulent viscosity μ_T is added to the laminar viscosity μ. The turbulent viscosity is related to mean flow variables by means of a mixing length distribution:

$$\frac{\mu_T}{Re} = \rho \ell^2 \left[2 \bar{\bar{e}} : \bar{\bar{e}} \right]^{\frac{1}{2}} \tag{19}$$

where $\bar{\bar{e}}$ is the mean flow rate of strain tensor:

$$\bar{\bar{e}} = \frac{1}{2} \left[\left[\nabla \bar{V} \right] + \left[\nabla \bar{V} \right]^T \right] \tag{20}$$

The mixing length, ℓ, was determined from the empirical relationship of McDonald and Camarata for equilibrium turbulent boundary layers and the modified Bushnell wake model, as follows.

The mixing length by McDonald and Camarata can be written:

$$\ell_1 \left[\tilde{y}\right] = 0.09\ \delta_b \tanh\left[\kappa\tilde{y}/\left[0.09\ \delta_b\right]\right] \cdot D \tag{21}$$

where δ_b is the local boundary layer thickness on the cross-plane, κ is the von Karman constant, taken as 0.43, $\tilde{y}$ is the distance from the trailing edge, and D is a sublayer damping factor defined by:

$$D = \frac{P^{\frac{1}{2}}(y^+ - \bar{y}^+)}{\sigma} \tag{22}$$

where P is the normal probability function, $y^+ = y(\tau/\rho)^{\frac{1}{2}}/(\mu/\rho)$, τ is local sheer stress, $\bar{y}^+ = 23$, and $\sigma = 8$.

In the wake region, the wake is due to the wake propagated from the upstream trailing line. The modified Bushnell wake model is used for evaluating the turbulent properties for its simplicity and accuracy (Ref. 6). The mixing length is estimated as follows:

$$\ell = 0.07\ \min\ (d_1, d_2) \tag{23}$$

where

$$d_1 = 0.48\ (d_o + 0.24x') + 0.15x' \tag{24}$$

$$d_2 = 0.96\ (d_o + 0.24x') \tag{25}$$

d_o is an estimate of the wake shear layer thickness at the trailing edge computed from an integral boundary layer calculation and x′ is the normal (helical) distance from the trailing edge to the computational plane.

A mixing length blending region was provided in the wake region near the trailing edge to insure the smooth transition of the mixing length.

Governing System of Equations

A complete system of five coupled equations governing U_p, Ω_n, ϕ, ψ, and P is given by Eqs. (8), (9), (10), (13) and (14). Ancillary relation Eq. (5) is given for the composite velocity. In Refs. 1 and 2, these equations are given in general orthogonal coordinates and in Ref. 3 in nonorthogonal coordinates.

Numerical Method

Since techniques for obtaining the basic inviscid flow solution are well known and numerous, they need not be enumerated or discussed here. Instead, the present development concentrates on describing the numerical method used to solve the system of governing equations. Streamwise derivative terms in the governing equations have a form such as $u_3 \partial(\ )/\partial x_3$, and because the streamwise velocity u_3 is very small in the viscous dominated region near no-slip walls, it is essential to use implicit algorithms which are not subject to stringent stability restrictions unrelated to accuracy requirements. Although it is possible to devise algorithms for solution of the governing equations as a fully coupled implicit system, such algorithms would require considerable iteration for the system of equations treated here, and this would detract from the overall efficiency. The present method is semi implicit and seeks to reduce the amount of iteration required and yet avoid the more severe stability restrictions of explicit algorithms. The method partitions the system of governing equations into subsystems which govern the primary flow, the secondary flow, and the turbulence model. The primary-flow subset of equations contains the streamwise momentum equation. The secondary-flow subset of equations contains the secondary vorticity equation, the scalar and vector potential equations and the pressure equation. These subsystems are decoupled by linearizing the solution variables in the spatial marching direction.

Summary of Algorithm

The governing equations are replaced by finite-difference approximations. Three-point central difference formulas are used for all transverse spatial derivatives. Analytical coordinate transformations are employed as a means of introducing a nonuniform grid in each transverse coordinate direction to concentrate grid points in the wall boundary layer regions. Second-order accuracy for the transverse directions is rigorously maintained. Two-point backward difference approximations are used for streamwise derivatives, although this is not essential.

The primary flow subsystem of viscous equations is solved via a scalar ADI scheme. In this application this is the streamwise momentum equation. Given the solution for the primary flow, the secondary flow subsystem can be solved. First, the scalar potential equation (continuity) is solved using a scalar iterative ADI

as a fully implicit coupled system and solved using an iterative linearized block implicit (LBI) scheme (cf. Briley and McDonald, Ref. 1). In selecting boundary conditions for the secondary flow subsystem, care must be taken to ensure that the final secondary velocity satisfies the no-slip condition accurately. Zero normal derivatives of ϕ are specified in the scalar potential equation, and this boundary condition corresponds to zero normal velocity. It is not possible to simultaneously specify the tangential velocity, however, and thus the ϕ-contribution to the secondary velocity will have a nonzero tangential (slip) component, denoted v_t, at solid boundaries. In the coupled vorticity and vector-potential equations, both normal and tangential velocity components can be specified as boundary conditions, since these equations are solved as a coupled system. By choosing (a) zero normal velocity, and (b) $-v_t$ as the ψ-contribution to the tangential velocity, the slip velocity v_t arising from the ϕ calculation is cancelled, and the composite secondary flow velocity including both ϕ and ψ contributions will satisfy the no-slip condition exactly.

A summary of the overall algorithm used to advance the solution a single axial step follows. It is assumed that the solution is known at the n-level x^n and is desired at x^{n+1}.

(1) The imposed streamwise pressure gradient distribution is determined from an <u>a priori</u> inviscid potential flow.

(2) The momentum equation is solved using an iterative scalar ADI scheme to determine u^{n+1}.

(3) Using u^{n+1} and the imposed pressure, the density is obtained from Eq. (17).

(4) Using values now available for u^{n+1}, the scalar potential equation (8) is solved using an iterative scalar ADI scheme to obtain ϕ^{n+1}. This ensures that the continuity equation is satisfied.

(5) The equations for vorticity (14) and vector potential (9) form a coupled system for Ω^{n+1} and ψ^{n+1}, which is solved as a coupled system using an iterative LBI scheme.

(6) Values for the transverse velocities v_s and w_s are computed from Eq. (3).

(7) Using the computed velocity field, the transverse pressure field is computed from Eq. (13) by an iterative scalar ADI scheme.

INCORPORATION OF INVISCID GRADIENT

The three-dimensional viscous primary/secondary flow analysis utilizes physical approximations which allow economical solution by a spatial marching algorithm. In the present application to aircraft propeller flows, these approximations employ computed results obtained from an inviscid panel code applied to the flow geometry of interest. The inviscid flow results are utilized in the viscous primary/secondary flow analysis in two ways: as part of the transverse velocity decomposition, and as streamwise pressure gradients imposed in the streamwise momentum equation. First, the transverse velocity decomposition is formulated as a correction to the transverse velocity components obtained from the inviscid panel code. The primary advantage of this technique is that it facilitates the treatment of far-field boundary conditions. Secondly, the imposition of streamwise pressure gradients from the panel code incorporates these potential flow accelerations within the spatial marching approximations.

The motivation for including the panel-code transverse velocity components in the velocity decomposition is as follows: although the outer (far field) computational boundary can optionally be located at a large distance from the blade tip region where the flow is essentially uniform with specified incidence, there are advantages to locating the outer boundary relatively close to the blade tip. This reduces the number of grid points needed in the cross-section. However, as the outer boundary is moved closer to the blade, the effects of viscous displacement interaction and of velocities induced by the tip vortex will modify the velocity field at the outer boundary. Consequently, the far field boundary conditions should be imposed in a way that correctly specifies the angle of incidence and also allows the velocity field to be perturbed by these effects of induced velocity and displacement interaction. The panel code transverse velocity components satisfy the angle of incidence conditions and include the effect of body surface geometry on the potential flow at the outer boundary. By expressing the present velocity decomposition as a correction to the panel code

velocities, these effects are imposed directly and the treatment of outer boundary conditions can focus on the effects of induced velocity and displacement interaction. The computed velocity correction is decomposed into two vector components, a scalar potential and a vector potential. The outer boundary conditions are specified as follows: the scalar potential is set to zero on the outer boundary, which implies its tangential velocity component is zero, but allows displacement interaction in its normal component of velocity. The vector potential is also set to zero on the outer boundary, which implies its normal velocity component is zero, but allows induced velocity in its tangential component of velocity.

The viscous spatial marching analysis provides a pressure field consistent with viscous effects and the tip vortex flow. This pressure field is computed in each two-dimensional cross-section as part of the solution procedure, and these results are linked together in the streamwise direction to form the three-dimensional pressure field. This streamwise linking is done by adjusting the pressure level in each two-dimensional cross-section to match the panel code pressure at a single point on the outer boundary, at each cross-section.

The present computer code has been modified to include a capability for utilizing potential flows computed by the panel code of Hess (Ref. 4). The procedure for interfacing the two codes is as follows: a coarse grid is generated using the same reference line and computational domain as that to be used in the fine mesh viscous flow calculation. The velocities and pressure on this coarse grid are computed as off-body points using the Hess panel code, and an output file containing the potential flow results is saved. A modification is needed in the region close to the airfoil surface to smooth the panel code results, which are not accurate when in close proximity to the surface singularities used as the basis of the panel code computation. This smoothing is accomplished by specifying the region to be smoothed next to the surface, and then extrapolating the panel code velocities and pressure from values outside the smoothing region. The (extrapolated) coarse grid results are then interpolated onto the viscous grid. The thickness of this region is governed by the transverse distance between grid points on the blade surface in the potential flow calculation and is typically 10% to 20% of chord.

The capability of the procedure for interfacing the Hess inviscid panel code with the viscous spatial marching analysis is demonstrated in SR3 flow calculations presented in a later section.

GEOMETRY SPECIFICATION

The SR3 geometry package and the PEPSIG/SR3 interface have been developed to facilitate the application of the forward marching code PEPSIG to the computation of viscous flows in the tip region of an advanced aircraft propeller blade such as the SR3 propeller blade.

Given the propeller blade geometry, PEPSIG/SR3 requires the choice of a reference line (i.e., a marching direction) and the construction of boundary conforming computational grids in planes normal to this reference line (the transverse coordinate planes). Therefore, the SR3 geometry package and the PEPSIG/SR3 interface must perform the following tasks:

(i) Define the geometry.
(ii) Define the reference line.
(iii) Construct the intersection of the propeller blade with a transverse coordinate plane.
(iv) Construct a boundary conforming grid in the transverse coordinate plane.

The tasks (i), (iii), and (iv) are performed by the SR3 geometry package, the task (ii) and the link between PEPSIG and the SR3 geometry package are part of the PEPSIG/SR3 interface.

A description of each of the tasks is given below.

Geometry Definition

The propeller blade geometry is defined by the (Cartesian) coordinates of a set of points on the blade, ordered such that they can be connected to form a "surface grid" on the blade. Spanwise ("airfoil") sections are ordered from hub to tip; points on an airfoil section are ordered from the bottom trailing edge via the leading edge to the top trailing edge of the section. These points can be read from an input file, or they can be constructed given information about the airfoil sections and the radial (spanwise) distribution of section properties (such as chord, thickness, twist angle, sweep angle, design lift coefficient, etc.). Figure 1 shows an example of a propeller geometry constructed in this

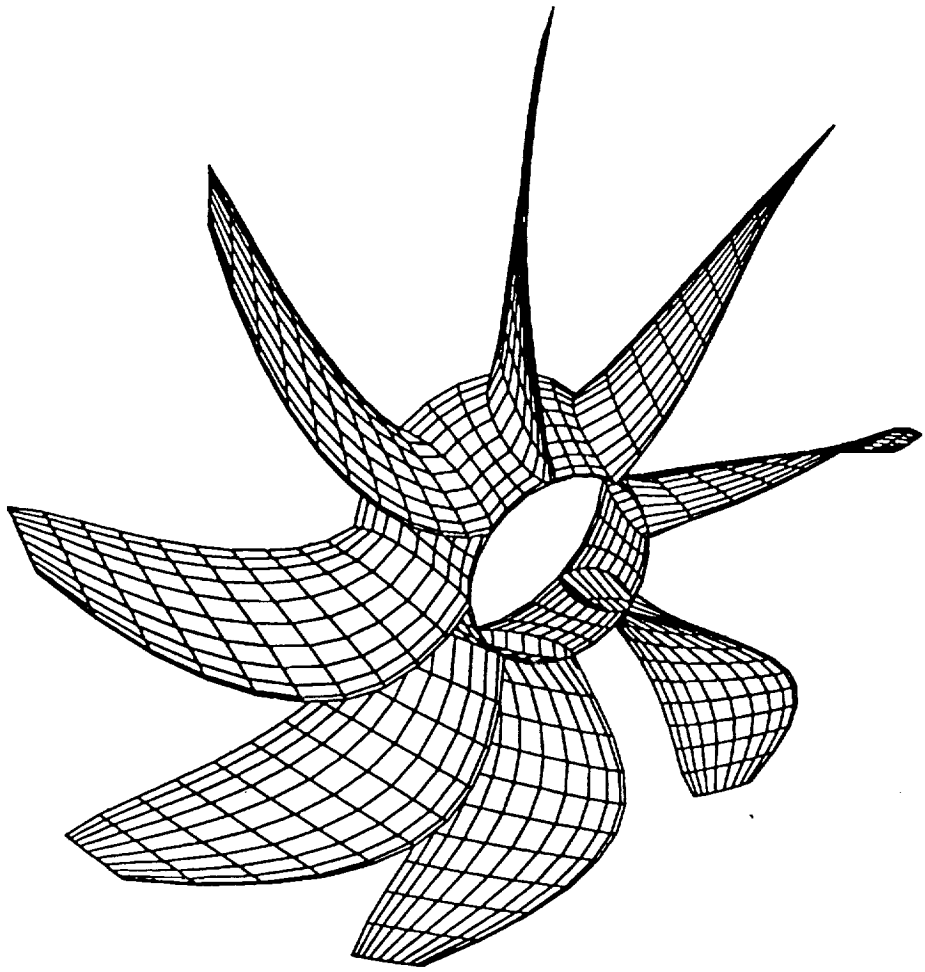

Figure 1. SR3-like Propeller.

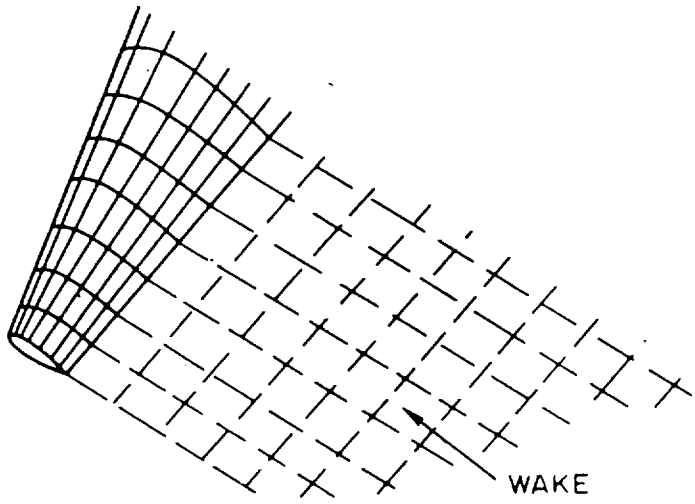

Figure 2. Wing/Wake Configuration.

manner using information given in NASA CR-3505 (Ref. 5). Here a "hub" and additional blades have been added for plotting purposes only.

After the geometry has been obtained, the airfoil sections and the points on each section can be redistributed using splines to get a more desirable surface grid. This is of importance for the construction of the intersection of a transverse coordinate plane and the propeller blade, and also for the use of this surface grid in a potential flow panel code.

In addition, to facilitate the generation of boundary conforming grids in transverse coordinate planes that intersect the blade trailing edge line, a geometric wake is constructed that bisects the (sharp) blade trailing edge at the trailing edge line and that tends to the helical surface determined by the design advance ratio of the blade at a large distance downstream of the blade. This (geometric) wake can also be used in the Hess panel code.

Finally, the blade/wake configuration can be transformed into a wing/wake configuration such that, at the design point, the local angle of incidence of each wing section is equal to the local angle of incidence of the corresponding (rotating) propeller blade section. Figure 2 shows the wing/wake configuration.

Qualitatively, the flow about the (non-rotating) wing is similar to the flow about the rotating propeller blade.

Reference Line Definition

Given the propeller blade geometry, an appropriate marching direction (reference line) can be chosen. Two obvious choices are:

(a) A helix through the tip trailing edge with an advance angle (Arctan (J)) equal to the design advance angle of the blade at the tip.

(b) A straight line through the tip trailing edge parallel to the tip section chord line or tangent to the tip helix, through the tip trailing edge.

The PEPSIG/SR3 interface allows either choice of reference line, if a straight reference line is chosen, its direction can be taken as in (b), or as an input.

Transverse Plane Intersections

Given the reference line, PEPSIG/SR3 defines a transverse coordinate plane at each point of this line such that the resulting coordinate system is orthogonal. Before a boundary-conforming grid can be constructed in a transverse coordinate plane, it is necessary to construct the intersection of this plane and the propeller blade/wake (or wing/wake) configuration. By transforming the coordinates into a Cartesian coordinate system whose x-axis is tangent to the reference line at the point under consideration, whose origin coincides with this point, and whose y- and z- coordinates correspond to the transverse coordinates, the problem of constructing the intersection can be reformulated to find the intersection of the blade/wake combination with the plane $x = 0$. This is done using spline-fits, under the assumption that each y-coordinate line intersects the blade/wake combination at most twice.

This condition is met for the configurations and reference-line coordinate systems under consideration. To illustrate the intersection generation capability, Fig. 3 shows intersections of the propeller blade/wake configuration of Fig. 1 with planes normal to the propeller axis. At the blade tip, the intersections have been augmented by a "cap", as shown in Fig. 4, to define a smooth surface with continuous derivatives. Figure 5 shows that intersections that contain the swept trailing edge of the blade look like airfoil sections. Figure 6 shows intersections of the tip region of the blade/wake configuration with transverse coordinate planes that correspond to a straight reference line through the tip trailing edge, parallel to the tip section chord line.

Grid Generation

Once the intersection of the transverse coordinate plane and the blade/wake configuration has been constructed, a boundary-conforming grid can be generated in the tip region. The grid generation procedure consists of two parts:

(1) Determine the extent of the computational domain.

(2) Construct a grid using an algebraic grid generation technique.

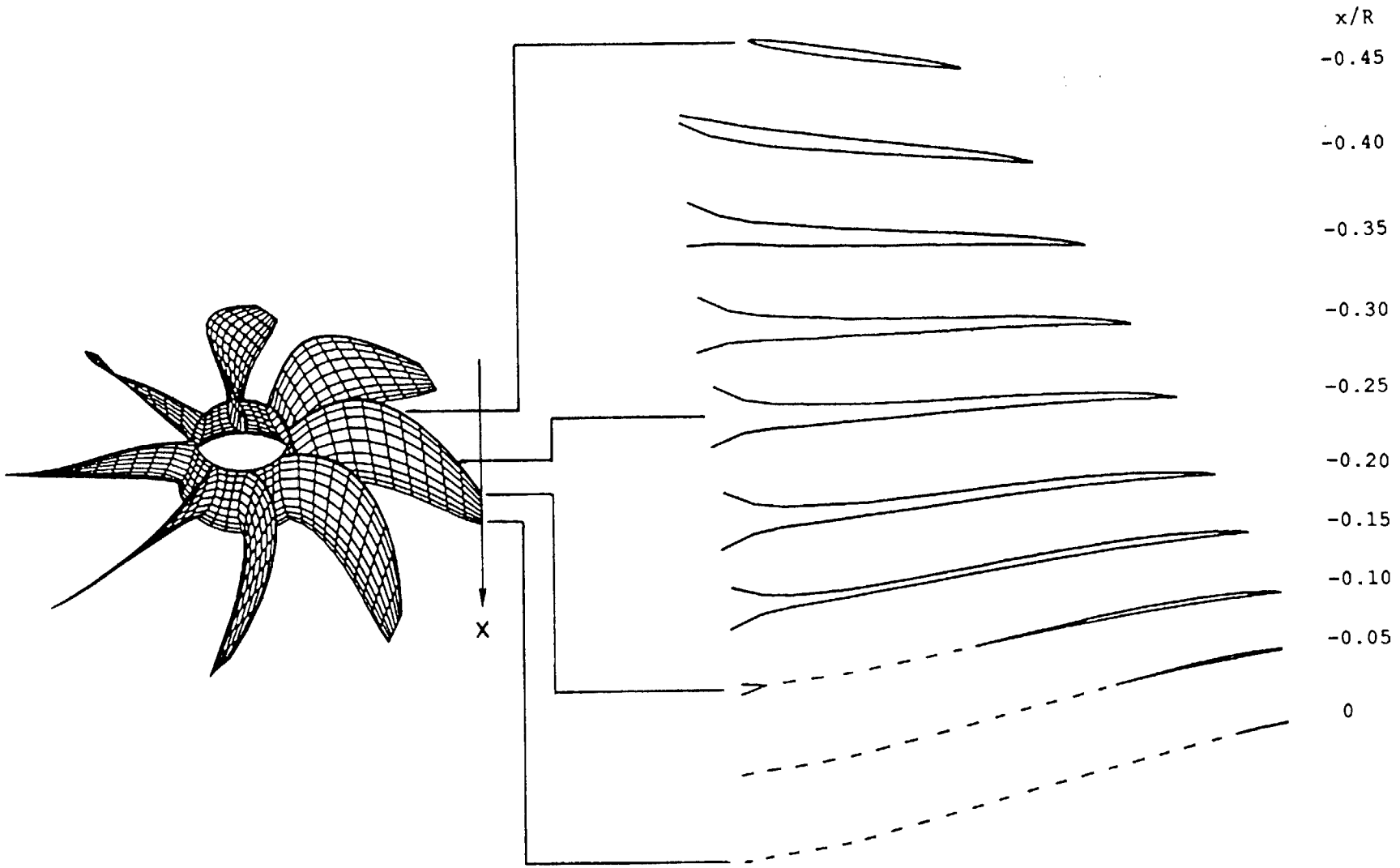

Figure 3. Intersections of the SR3-like Propeller Blade/Wake Configuration with Planes Normal to the Propeller Axis.

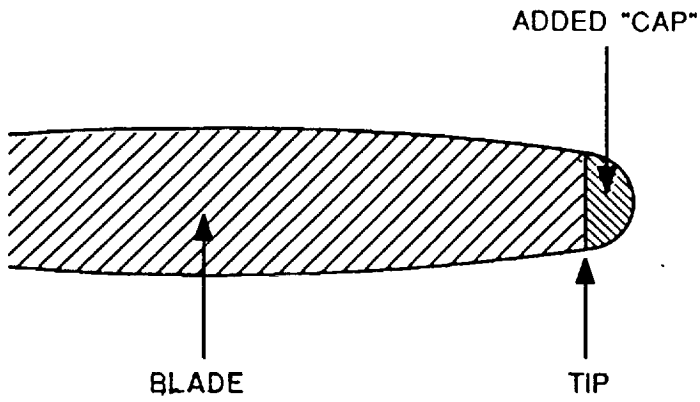

Figure 4. Addition of a Rounded Tip.

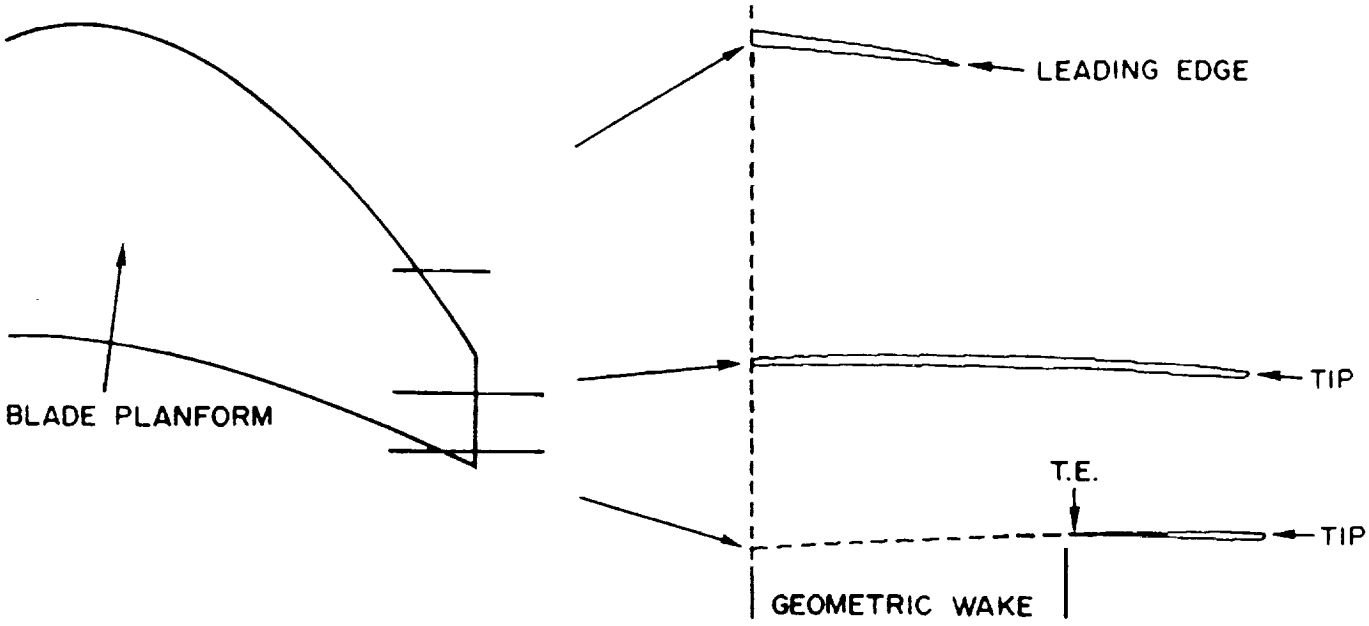

Figure 5. Types of Intersections of the Blade with Transverse Coordinate Planes.

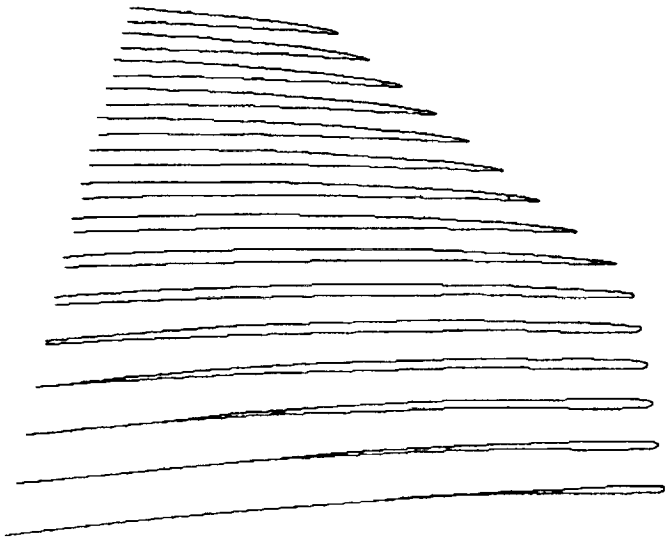

Figure 6. Intersections in the Tip Region of the SR3-like Propeller Blade/Wake Configurations with Planes Normal to the Tip Section Chord Line.

The extent of the computational domain is determined by locating an "inboard boundary" and "outer boundary", as shown in Fig. 7. The outer boundary consists of a semi-circle with center B and radius r and two straight line segments of length α that make and angle β with the z-coordinate line of the transverse y,z-coordinate system. The inner boundary is a straight line. The point B should be chosen near the leading edge or tip part of the blade, while the angle β should be a measure of the average angle that the blade makes with the z-coordinate. These conditions are not necessary, but they facilitate the construction of a suitable grid. The PEPSIG/SR3 interface provides estimates for the location of B and the angle β based on the choice of the reference line and the blade geometry in the tip region. The radius, r, and the distance, d, should be chosen sufficiently large so that the flow in the tip region can be computed without too much interference from the grid boundaries.

The construction of the boundary-conforming grid is governed by the condition that the resulting grid should be "smooth". Consider the situation shown in Fig. 8. The intersection shown consists of a wake piece and a body piece, and the grid construction proceeds as follows:

(1) Determine the intersection of the wake piece and the inboard boundary (coinciding points A and D on the "bottom" and "top" part of the wake).

(2) Spline-fit the "bottom" part of the wake, AB, the body piece, BC, and the "top" part of the wake, CD, using parameters that retain continuity across B and CD and generate identical wake parts AB and CD.

(3) Determine the grid point distribution on the line ABCD. Clustering will in general be required near the tip. Use symmetry to ensure that the grid points on AB coincide with those on CD. Smoothness across B and C is automatic because the wake and body pieces are treated simultaneously.

(4) Define the points F and G on the outer boundary such that the line FB is parallel to the inboard boundary and passes through the trailing edge point of the intersection (the coinciding points B and C).

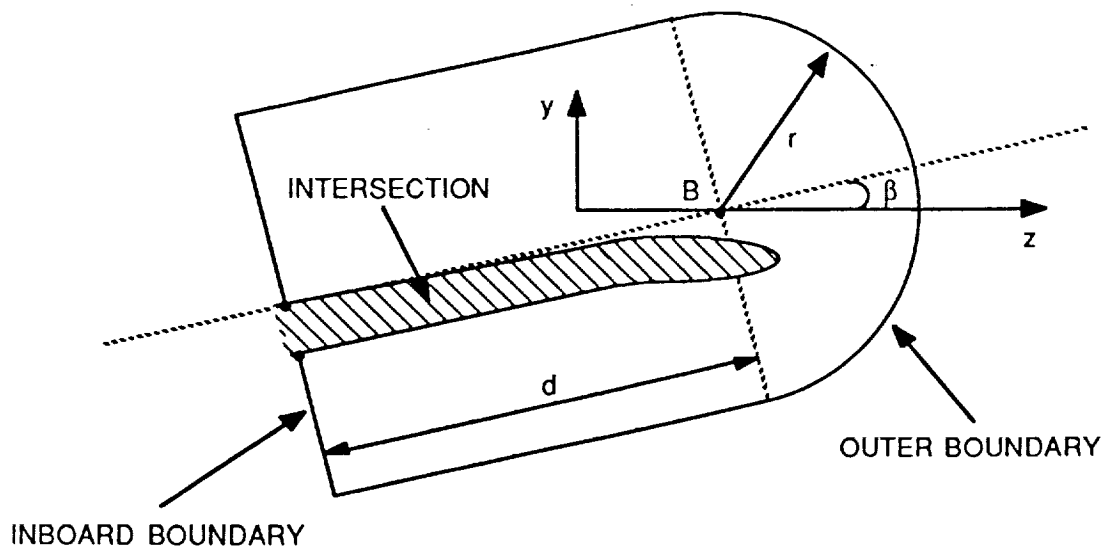

Figure 7. Extent of the Computational Domain in a Transverse Coordinate Plane.

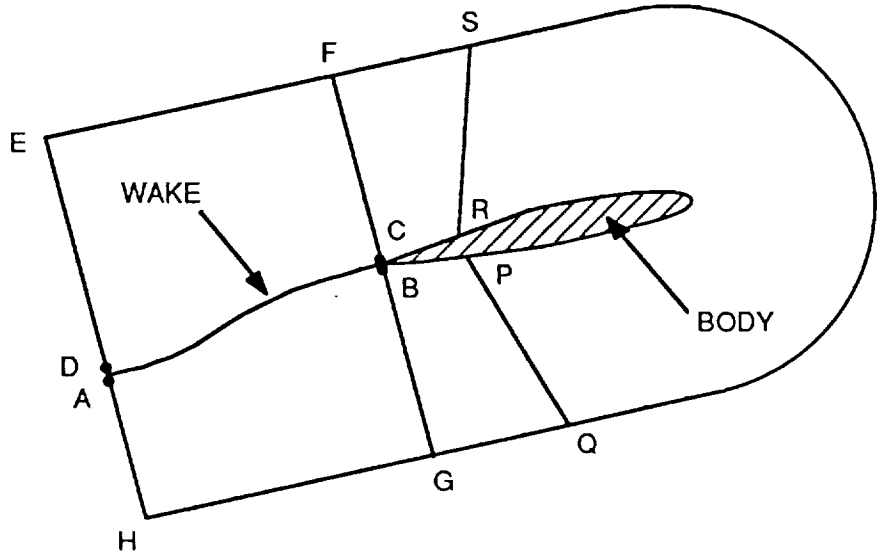

Figure 8. Construction of a Boundary-Conforming Grid.

(5) Determine the grid point distributions on the outer boundary pieces EF and HG by finding the intersection points of these pieces with the lines parallel to the inboard boundary and through the grid points on AB (or CD). This procedure guarantees grid base smoothness across the wake when grid points on the outer boundary are connected to grid points on the inner boundary (i.e., the boundary ABCD) by straight line segments.

(6) Determine the grid point distribution on the curved part FG on the outer boundary such that the overall grid point distribution on the outer boundary is sufficiently smooth; for example, continuity of the first and second derivatives of the grid point distribution at F and G can be guaranteed by using a 5-th order polynomial distribution function along FG. If a 7-th order polynomial distribution function is used, the mesh spacing at a point midway between F and G can be specified as well.

(7) Connect points on the outer boundary to corresponding points on the inner boundary by straight lines.

(8) Determine the grid point distribution on a pair of symmetrically located grid lines, such as PQ and RS in Fig. 8, by using a smooth distribution versus arc-length for the combined line QPRS (without a gap between P and R). Clustering can be included near P (or R). This procedure guarantees a smooth distribution of grid points across the wake piece, and also a smooth change of the distribution across the lines GB and FC.

The grid contribution procedure outlined above guarantees grid smoothness. A finite (i.e., nonzero) trailing edge angle at B (C) will lead to a grid singularity at the trailing edge point. Figure 9 shows sample grids for the cross-sections shown in Fig. 6.

SR3 CALCULATIONS AND DISCUSSION

An SR3 advanced aircraft propeller blade generated by the geometry package was used for the tip vortex flow computation. The advance ratio of the blade was 3.06. Figure 10 shows the plan view of the computational domain. A cross-section

Figure 9

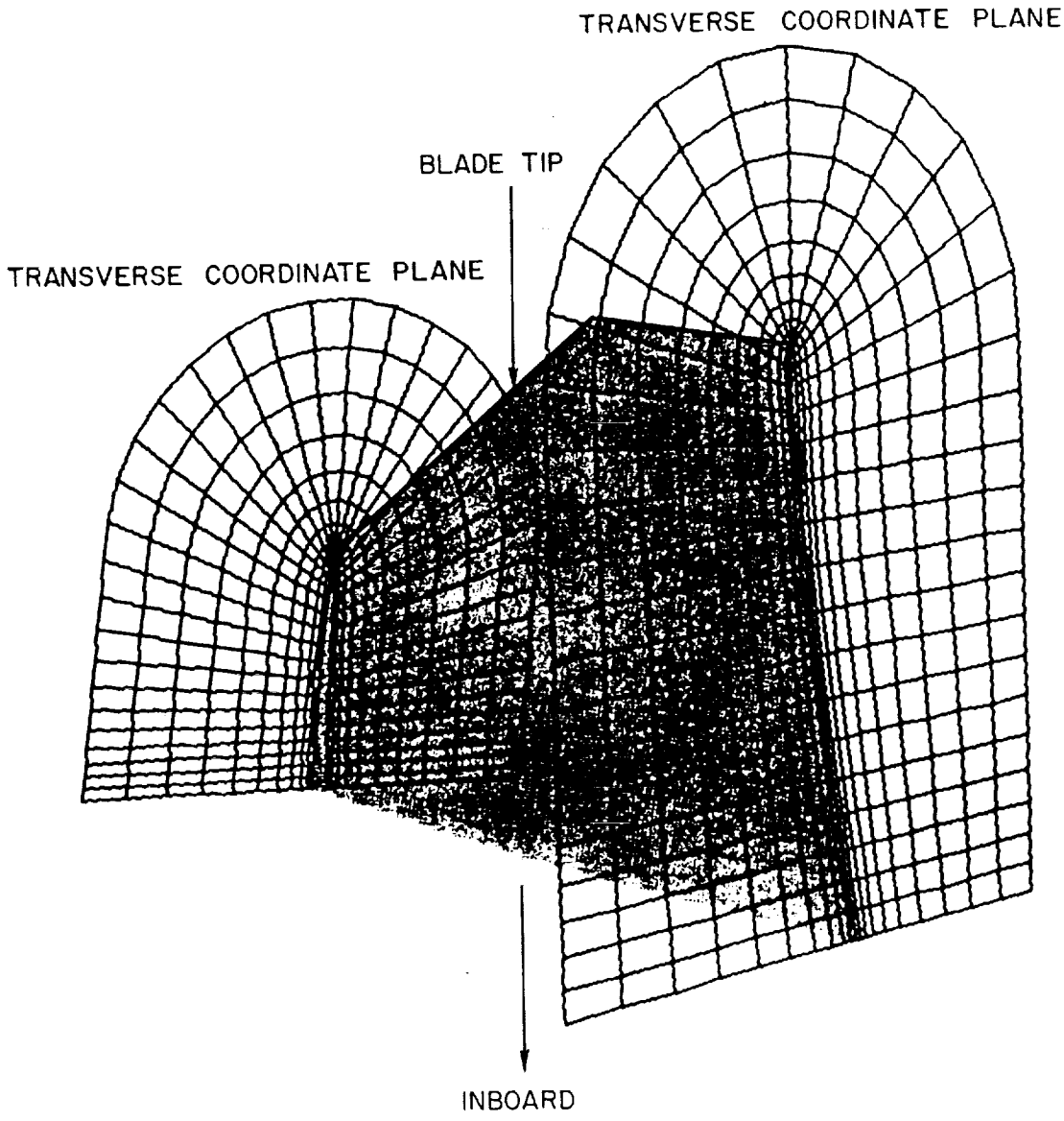

Figure 9. Coarse Grids in Planes Normal to the Tip Section Chord Line.

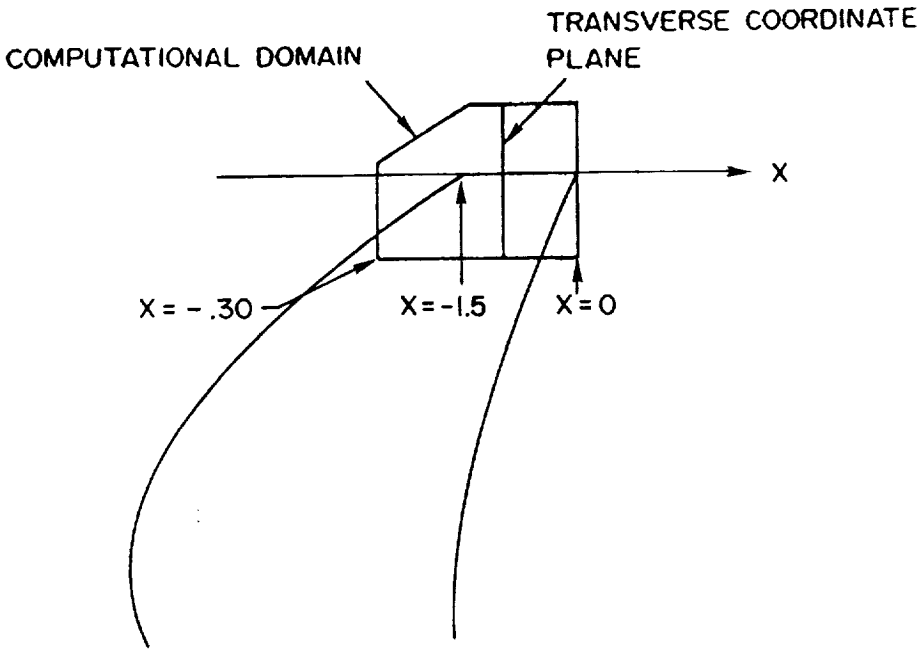

Figure 10. Plan view of blade and computational domain.

of the blade and the computational grid at a typical streamwise station are shown in Fig. 11. Both laminar and turbulent flow calculations were performed.

A laminar flow solution was computed at 8° angle of attack. The Reynolds number was 20,000 based on the reference length, R (the propeller radius). The free stream Mach number was 0.3 and the initial boundary layer thickness was 0.002 R at the initial station. The blade trailing edge was extended aft at zero thickness. The cross-plane grid was 49 x 49. Seventy-eight streamwise stations were used for the computation. Grid points were clustered near the propeller surface and in the tip region, where high flow gradients occurred. The distance of the first mesh line to the blade surface was about 10^{-5}. No slip and no penetration boundary conditions were imposed on this blade extension. The flow calculation was started at $x/R = -.30$, on the sloped leading edge of the blade as shown in Fig. 10. This case was run without a potential pressure field.

The flow development is shown in Figs. 12a through 12h in contour plots of streamwise velocity and secondary velocity plots in planes normal to the tip chord. In these planes, the angle of attack causes strong local accelerations at the tip as seen in the vector plots. Figure 12b shows evidence of the start of a vortex on the sloped leading edge of the blade. The vortex intensified as the boundary layer from the pressure side is convected into the vortex. Figures 12a through 12e are on the sloped leading edge of the blade. The vortex was seen to be strongly developed before the straight tip of the blade.

The above laminar flow case was also run at an infinite advance ratio. A perspective view of the blade tip region is shown in Fig. 13. The computational grid and the cross-section of a typical blade tip at a streamwise location are shown in Fig. 14. A 69 x 69 cross-plane mesh and three-hundred streamwise stations were used for the computation. The distance between the blade surface and the next circumferential grid line was about 3.6×10^{-6} R. The spanwise extent of the blade within the computational domain was twice of the previous case. The rest of the flow parameters remained the same. This case was also run without a potential flow pressure field.

Figure 15 shows the development of the tip vortex. On the right hand side, the secondary flow vector plots are presented and on the left hand side, the corresponding primary velocity contours. A comparison of Figs. 15 and Fig. 12 shows similar flow mechanisms, but different degrees of tip vortex intensity due to the different advance ratios of the blade. The mechanisms are the transport of the low momentum fluid from the pressure side boundary layer to the suction side

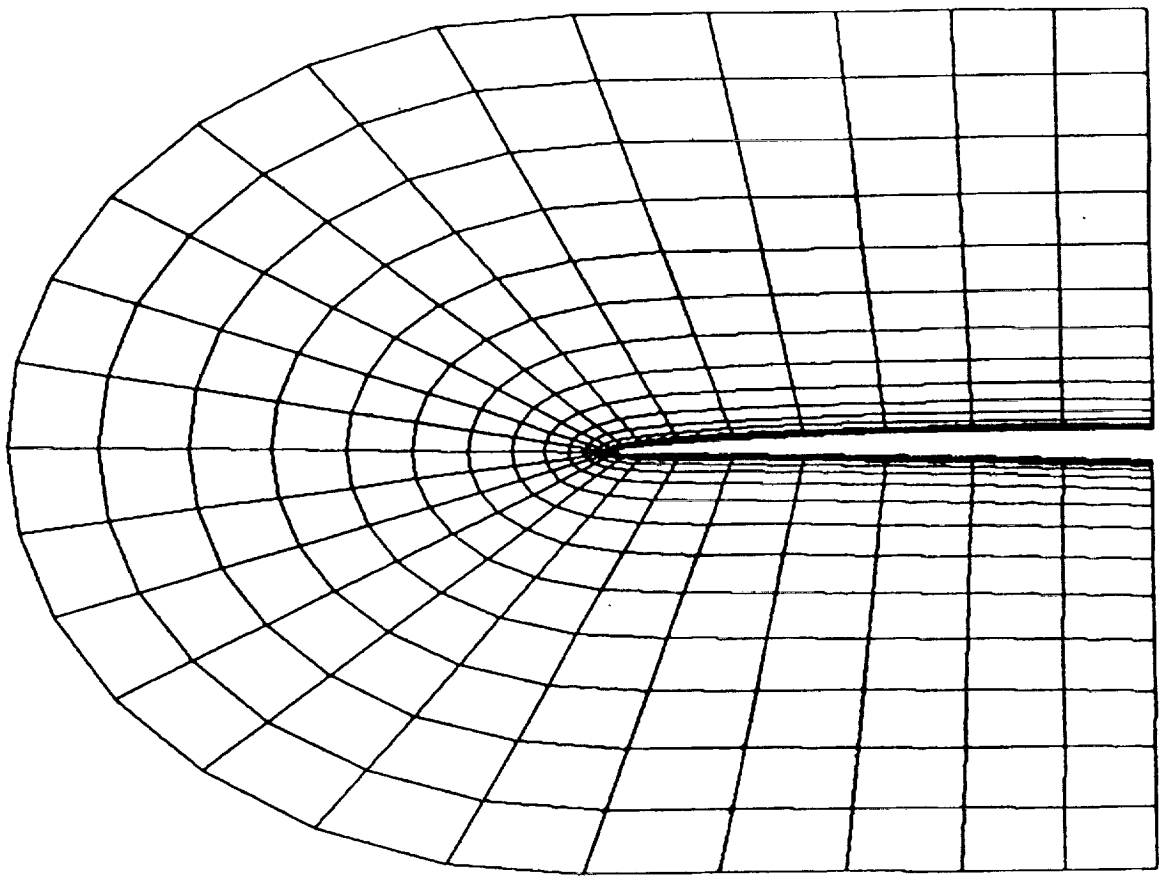

Figure 11. Cross-plane grid and cross-section of SR3 propeller blade tip at a typical station.

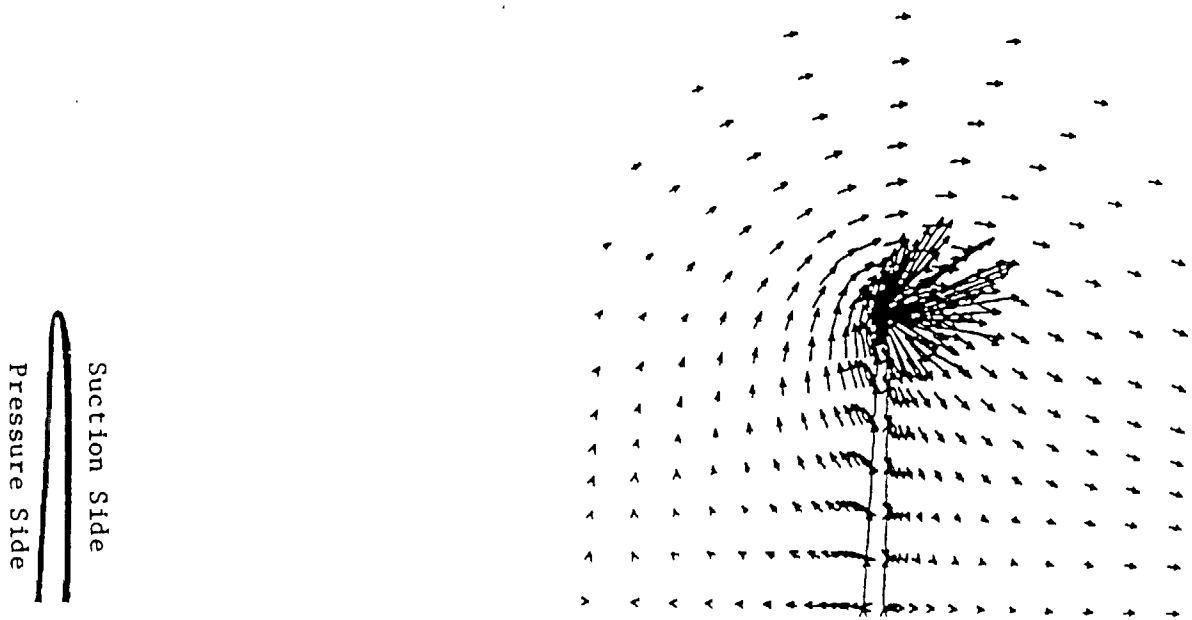

Figure 12a. Streamwise velocity contours and cross-flow velocity vectors in planes normal to the tip chord. (x = -0.300).

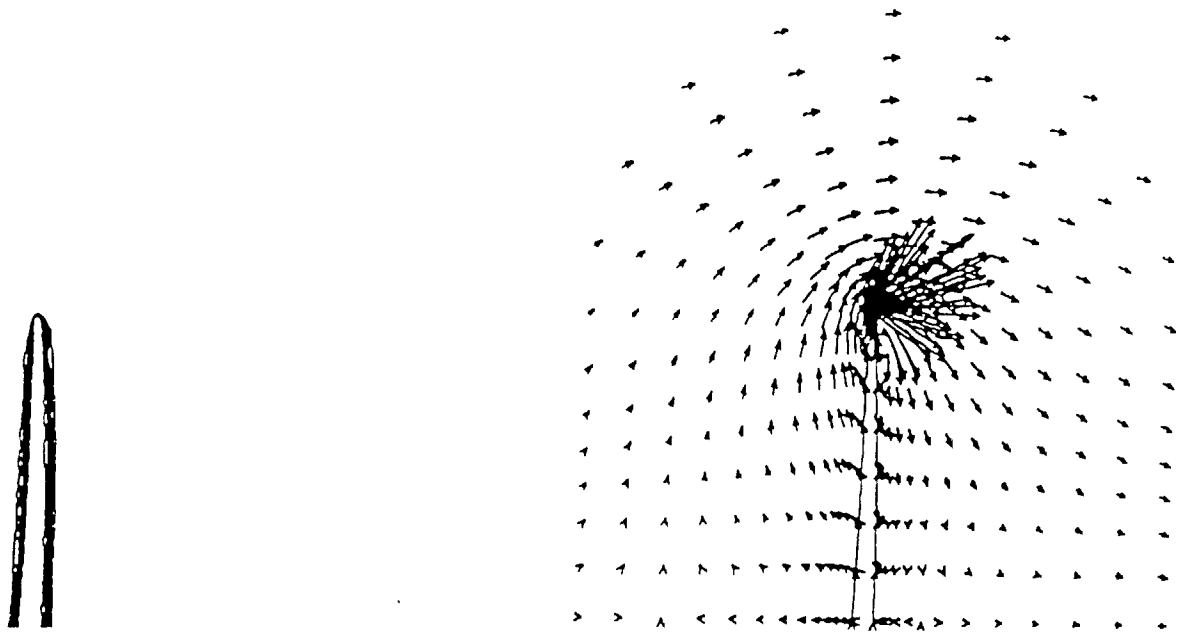

Figure 12b. Streamwise velocity contours and cross-flow velocity vectors in planes normal to the tip chord. (x = -0.287).

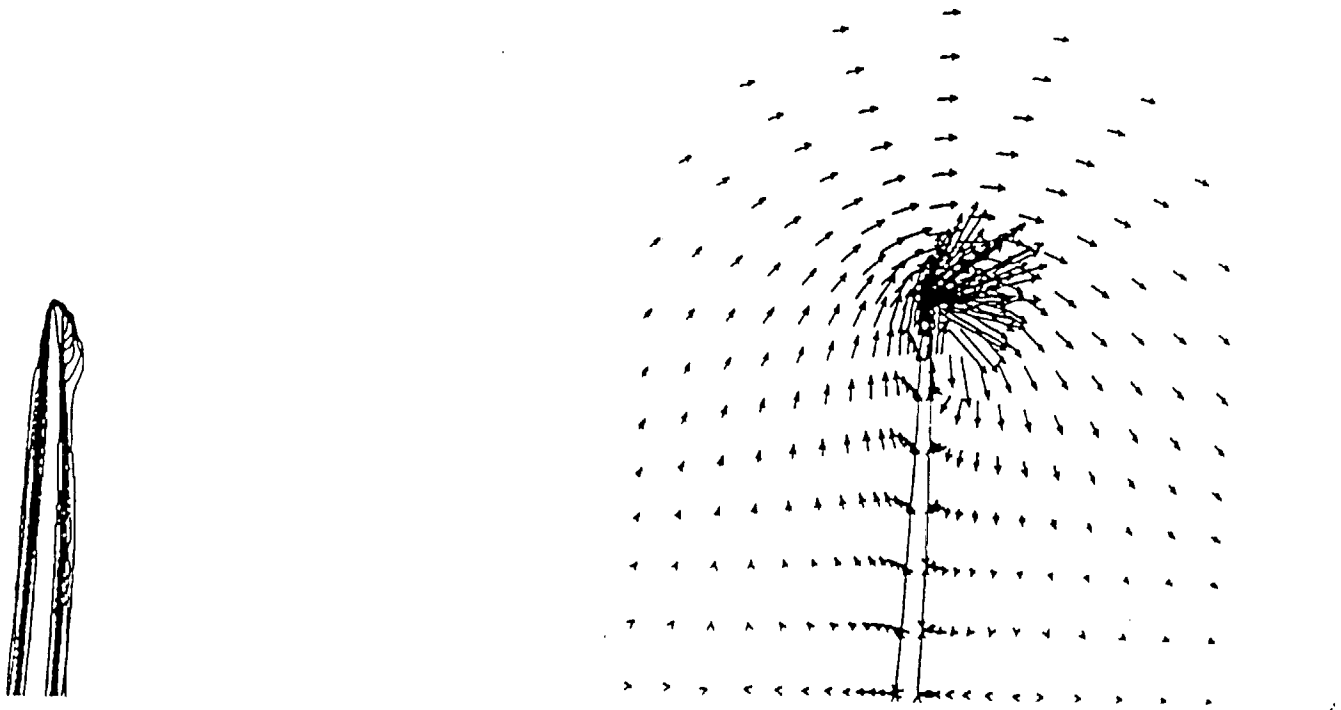

Figure 12c. Streamwise velocity contours and cross-flow velocity vectors in planes normal to the tip chord. (x = -0.246).

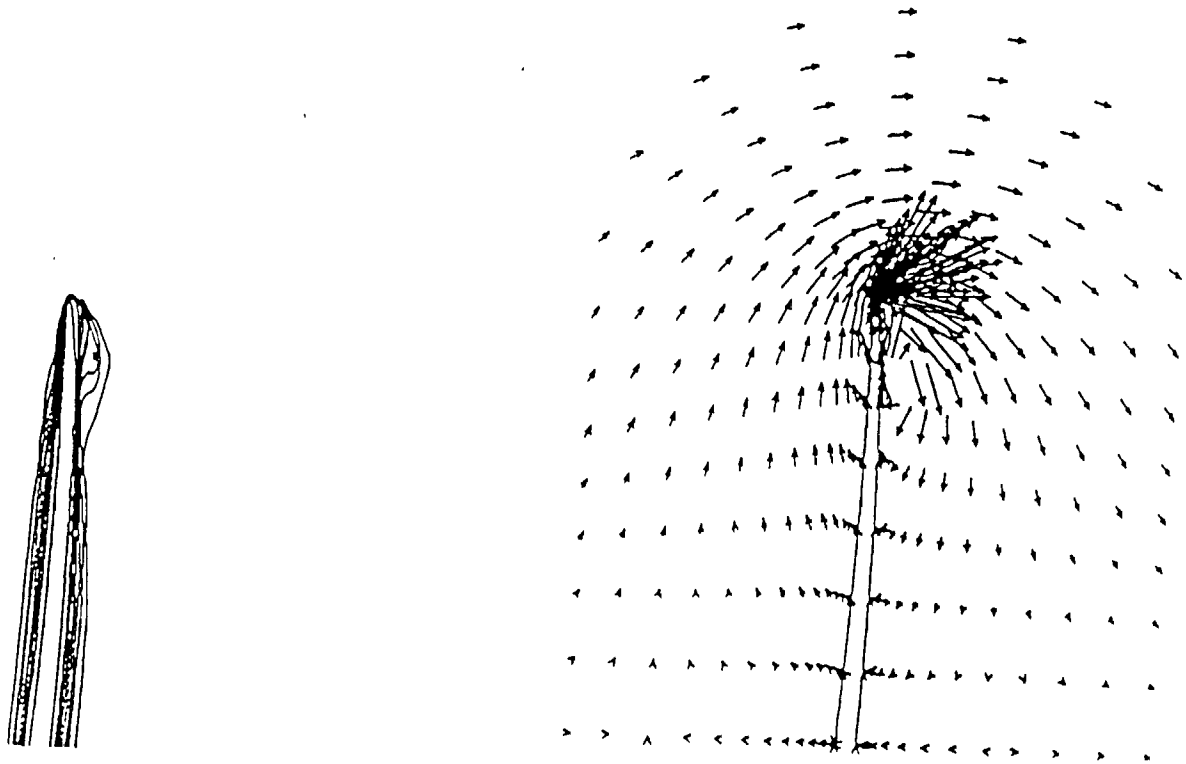

Figure 12d. Streamwise velocity contours and cross-flow velocity vectors in planes normal to the tip chord. (x = -0.215).

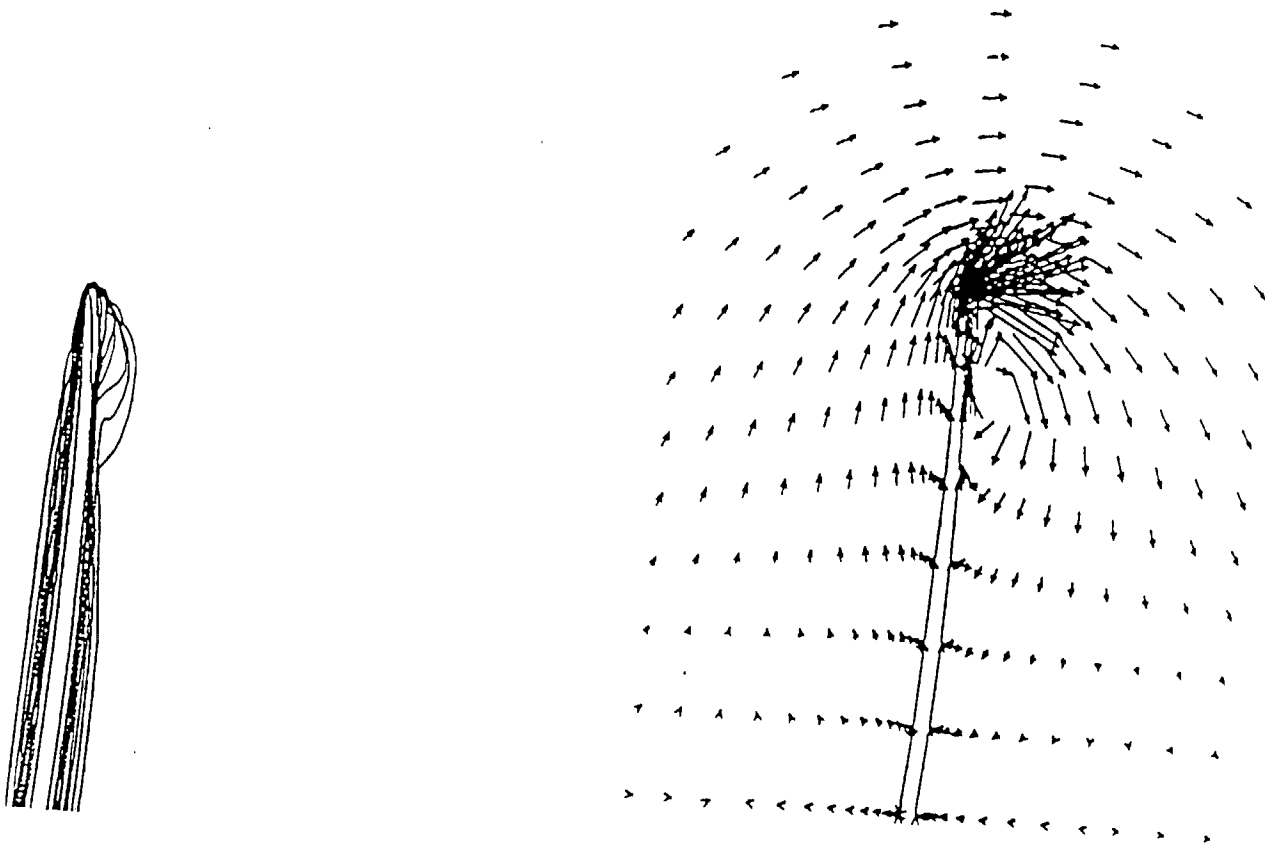

Figure 12e. Streamwise velocity contours and cross-flow velocity vectors in planes normal to the tip chord. (x = -0.173).

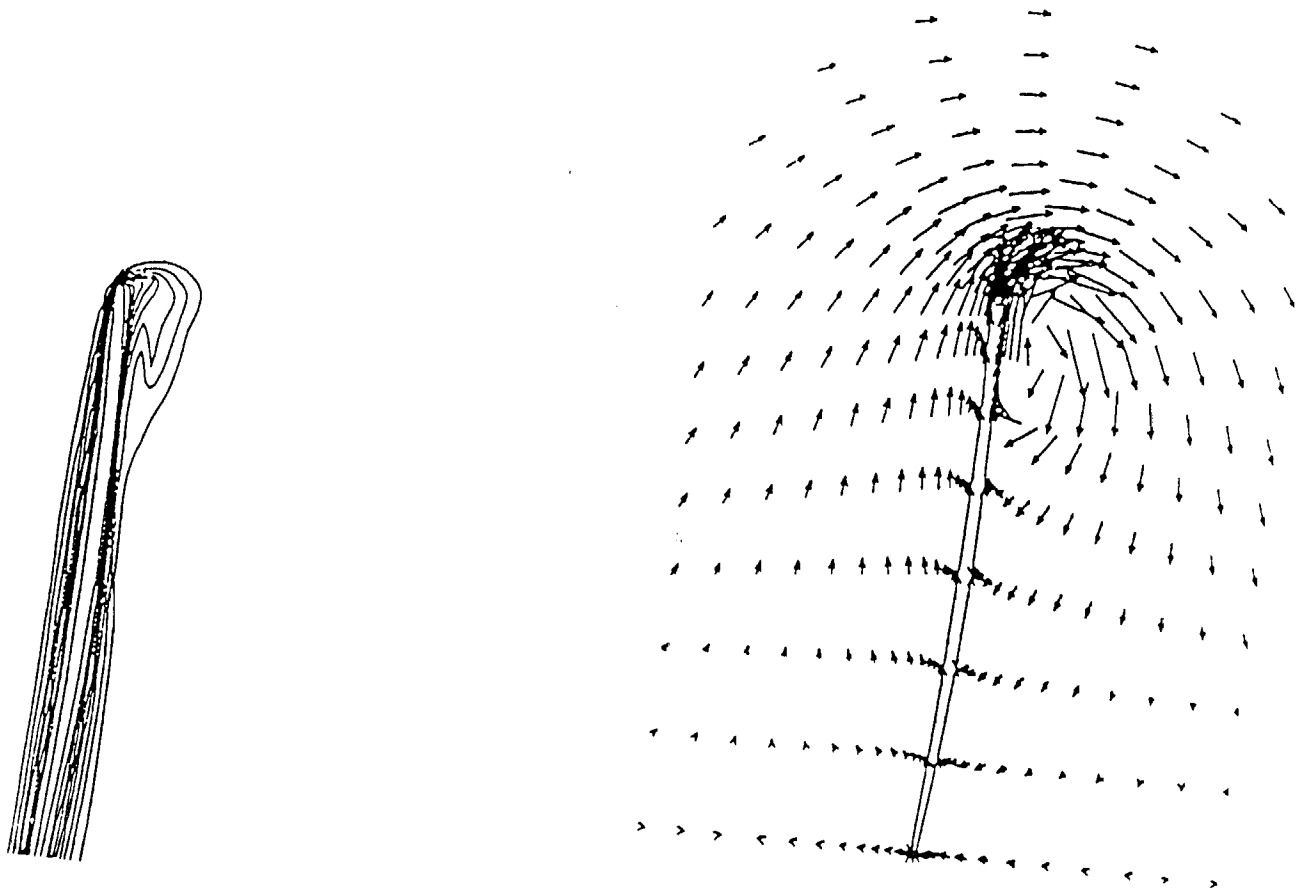

Figure 12f. Streamwise velocity contours and cross-flow velocity vectors in planes normal to the tip chord. (x = -0.116).

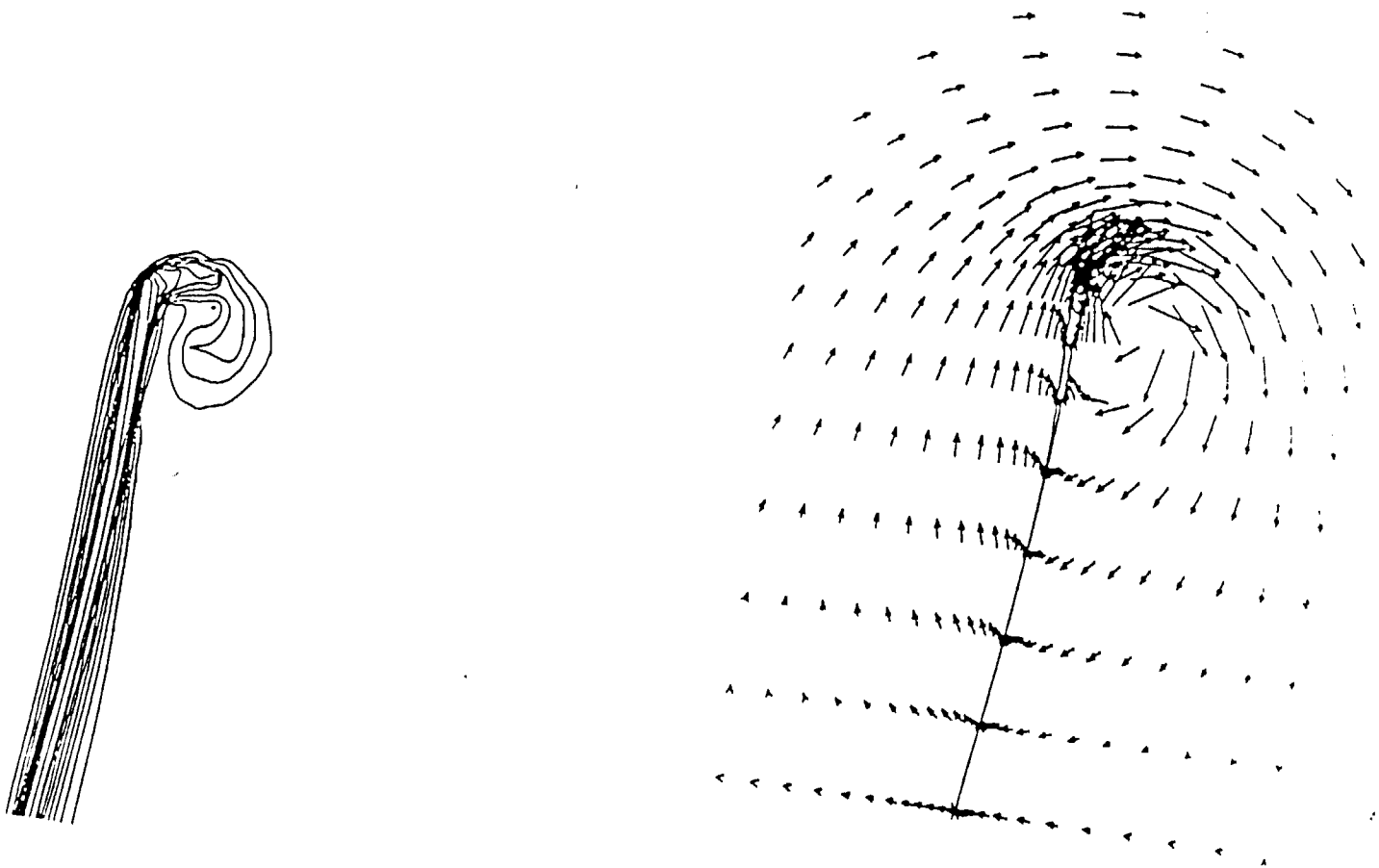

Figure 12g. Streamwise velocity contours and cross-flow velocity vectors in planes normal to the tip chord. (x = -0.040).

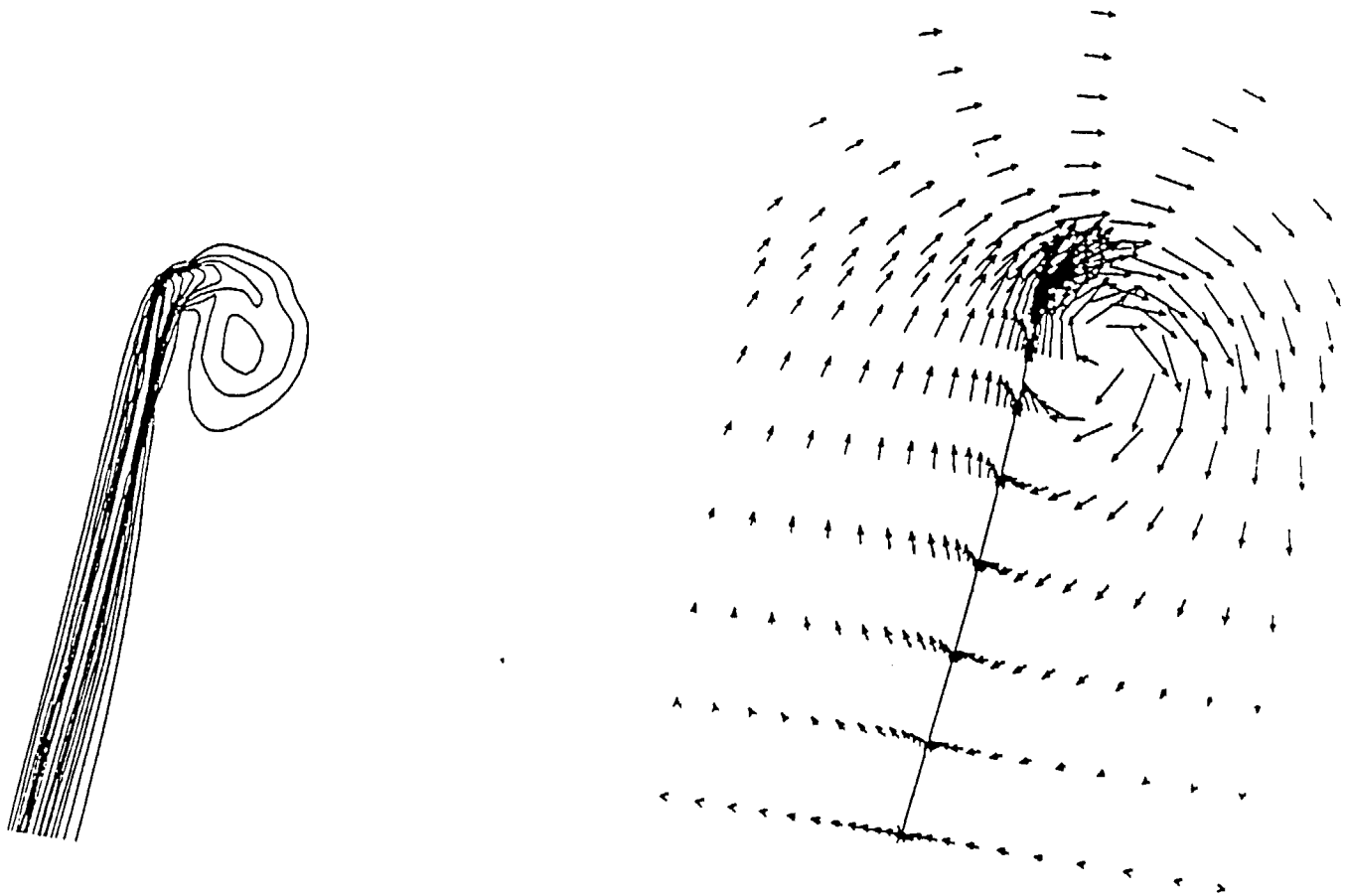

Figure 12h. Streamwise velocity contours and cross-flow velocity vectors in planes normal to the tip chord. (x = -0.013).

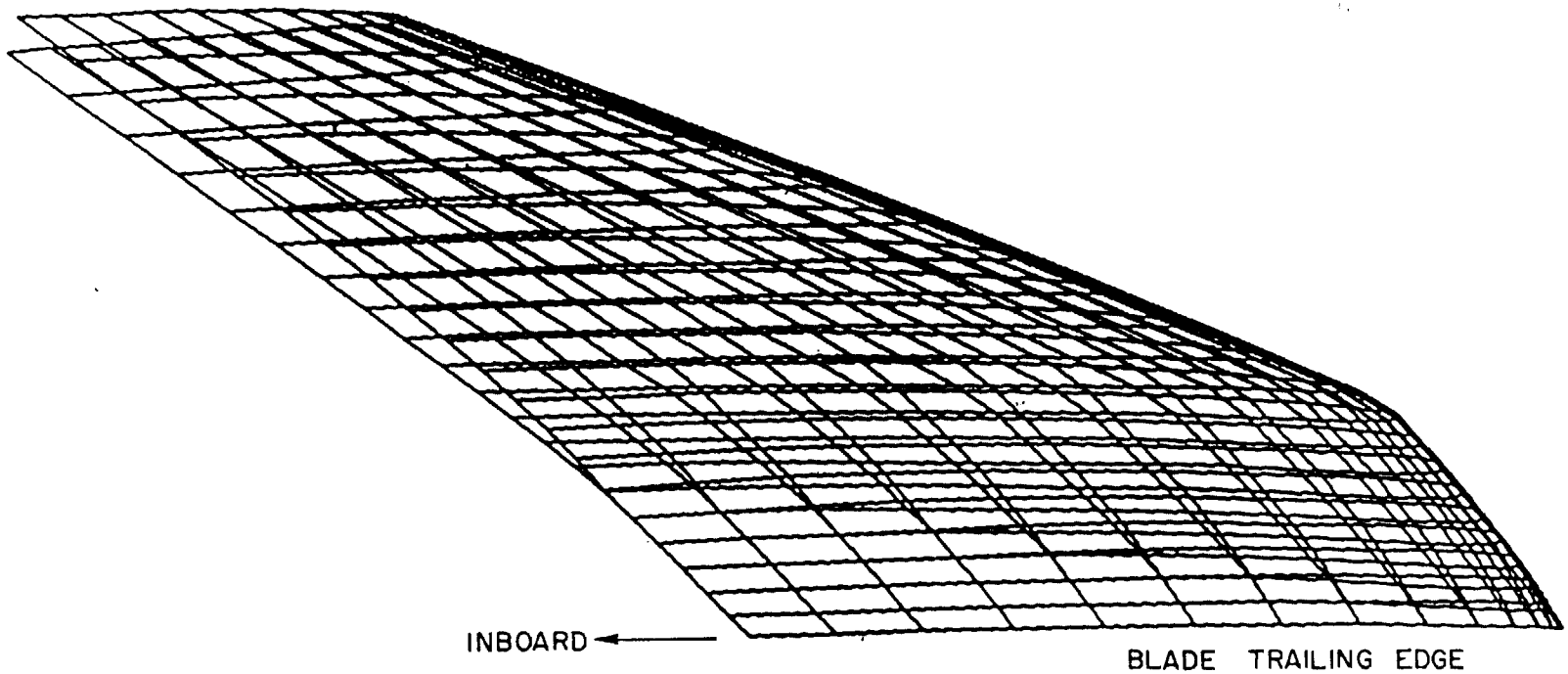

Figure 13. A perspective view of a SR3 blade tip with advance ratio of infinity.

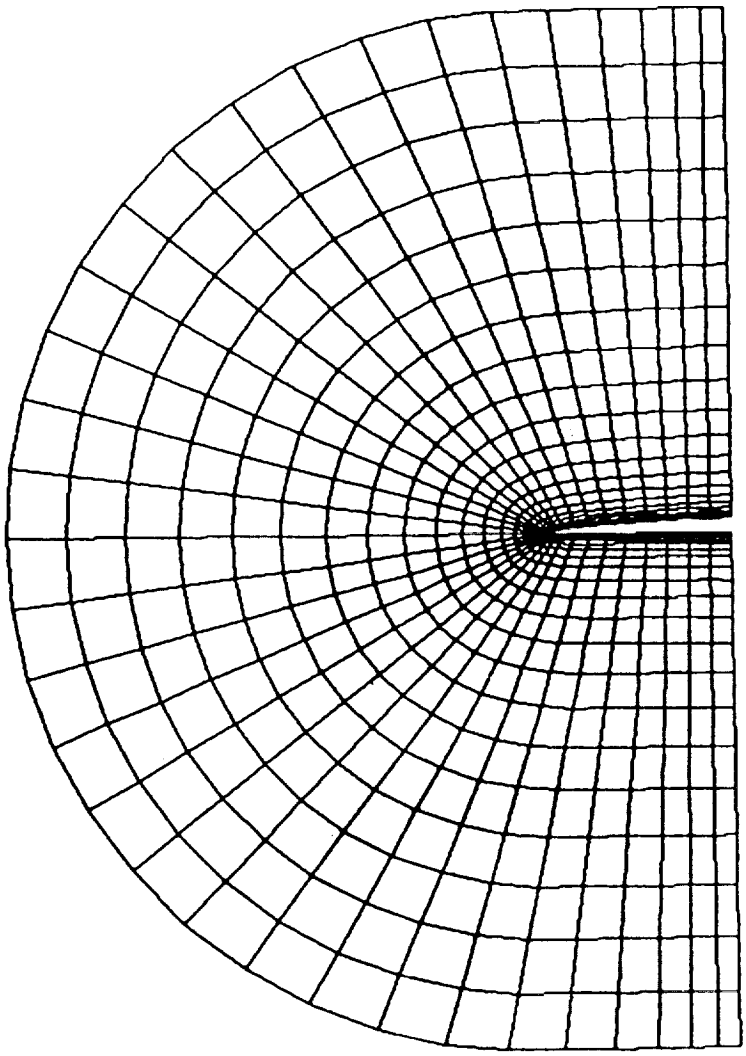

Figure 14. Cross-plane grid and cross-section of SR3 blade tip at a typical station.

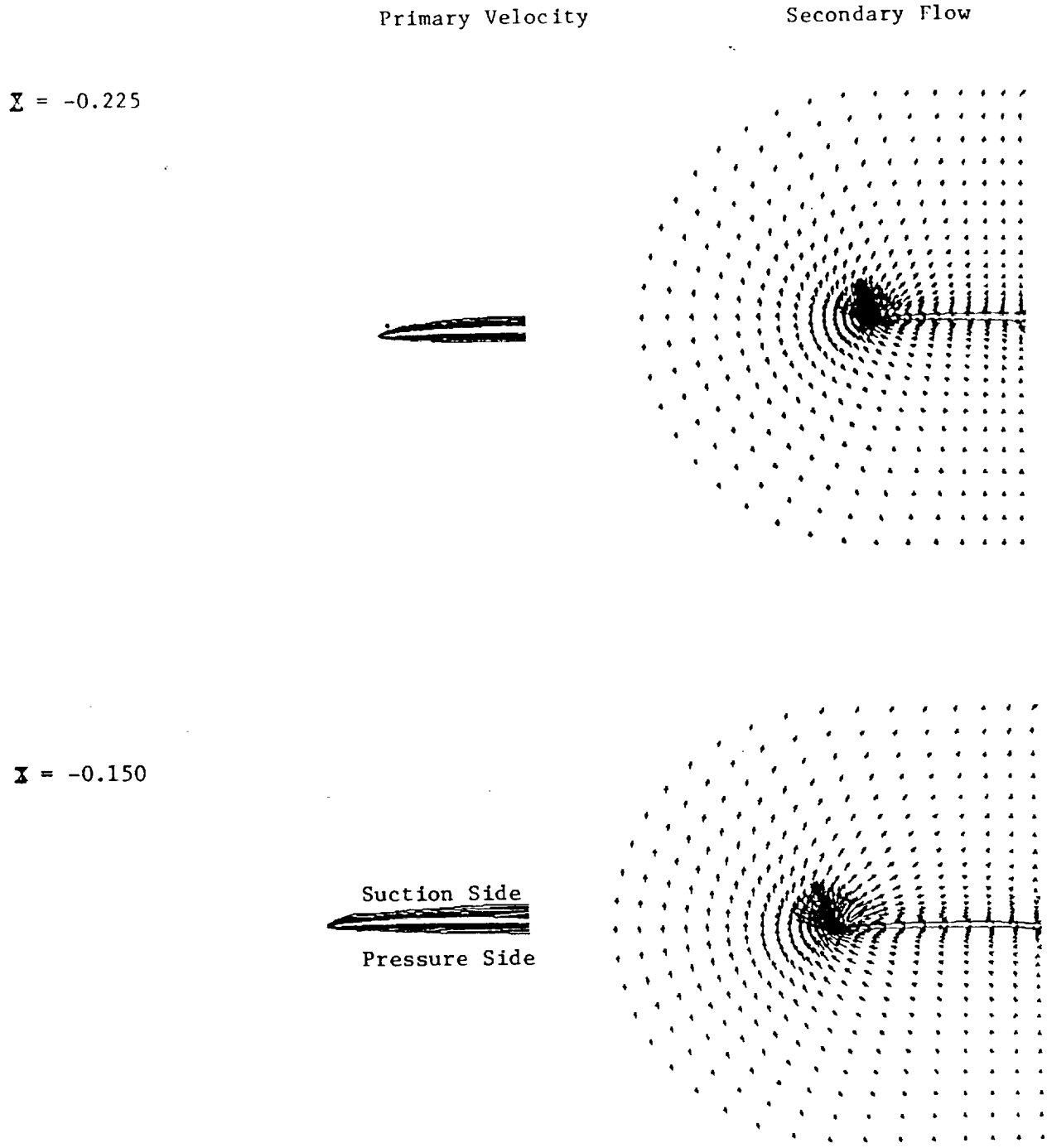

Figure 15a. Tip vortex development in the tip region of a SR3 blade without inviscid flow field. Re = 2×10^4.

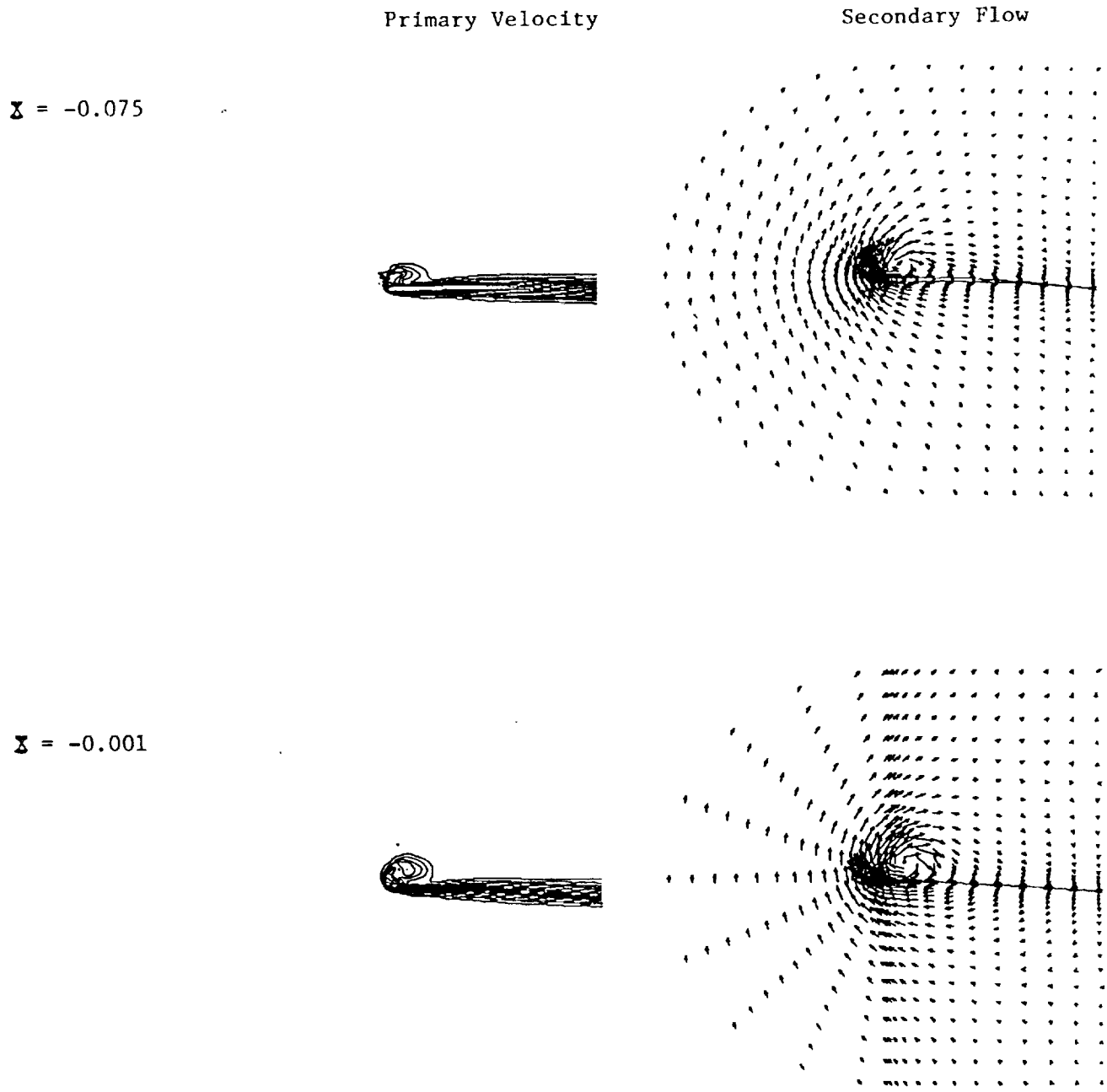

Figure 15b. Tip vortex development in the tip region of a SR3 blade without inviscid flow field. Re = 2×10^4.

by the transverse velocity, the accumulation of the low momentum fluid on the suction side, and the roll-up of the accumulated fluid into the tip vortex.

A turbulent case was computed for a blade with an SR3 plan form and 6% thickness at the tip. A potential flow solver, the Hess code developed by the Douglas Aircraft Company, was used to compute the inviscid flow field. The advance ratio of blade was infinity. A perspective view of this thicker blade tip geometry is shown in Fig. 16. The inviscid flow field obtained was further interpolated into the viscous grid and accessed for the viscous tip vortex flow calculated as described above. A 95 x 95 cross-plane grid and a total of three-hundred computational stations were used. The radial interval between the blade surface and the next circumferential grid line was about 2×10^{-6}. The Reynolds number was 3×10^{5}. The other flow parameters were the same as the previous case.

A mixing length type algebraic eddy viscosity model detailed above was used for the effects of turbulence. The computed solution in terms of the primary velocity contours and the secondary velocity vector plots at four streamwise stations at $x/R = -0.225$, -0.150, -0.75, and -0.001 are shown in Fig. 17. Blade twist and thickness distribution can be seen in these figures. An overview of the figures shows the development of the tip vortex. At $x/R = -0.225$ and -0.150, the streamwise velocity contours show little change of the initial boundary layer on the blade surface. The boundary layer is thinnest near the tip. The secondary velocity field around the tip convects low momentum fluid in the boundary layer on the pressure side around the tip onto the suction side. An indication of this process can be noted at $x/R = -0.075$. The thickening of the boundary layer on the suction side of the tip is due to the accumulation of low momentum fluid from the pressure side convected by the secondary velocity. The gradual accumulation of the low momentum fluid on the suction side causes the fluid to roll up into the tip vortex. This roll-up of the flow into the tip vortex is characterized by the "bulge" in the streamwise velocity contours on the suction side of the blade tip at $x/R = -0.001$. The extent of the bulge in the velocity contours indicates the core of the tip vortex.

As a comparison, the same turbulent case was computed using the potential flow pressure field. Figure 18 shows the streamwise contour plots and the secondary vector plots at two streamwise stations at $x/R = -0.75$ and -0.001. The flow pattern shows very little difference with respect to the case accessing the potential flow field. The tip vortex flow calculation without inviscid flow

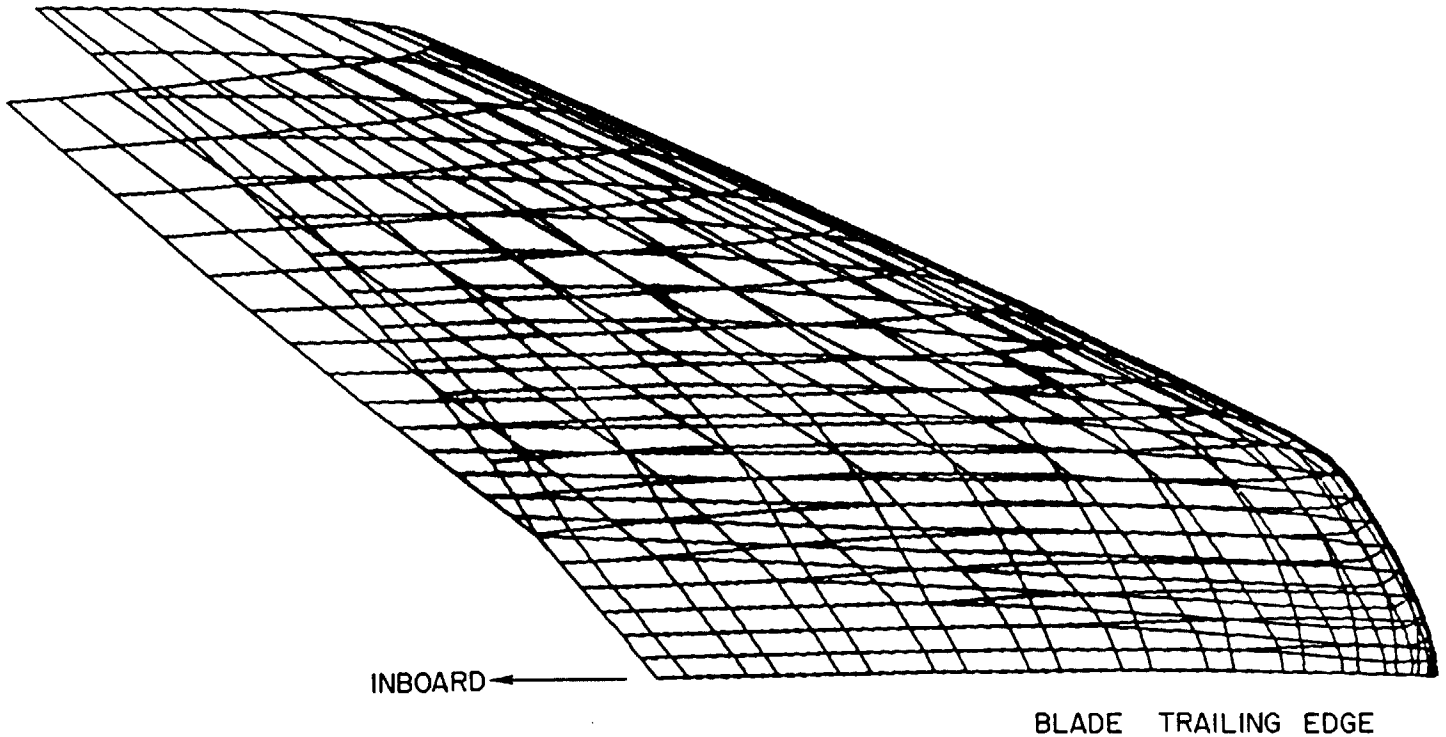

Figure 16. A perspective view of a SR3 blade tip with advance ratio of infinity. (6% thick).

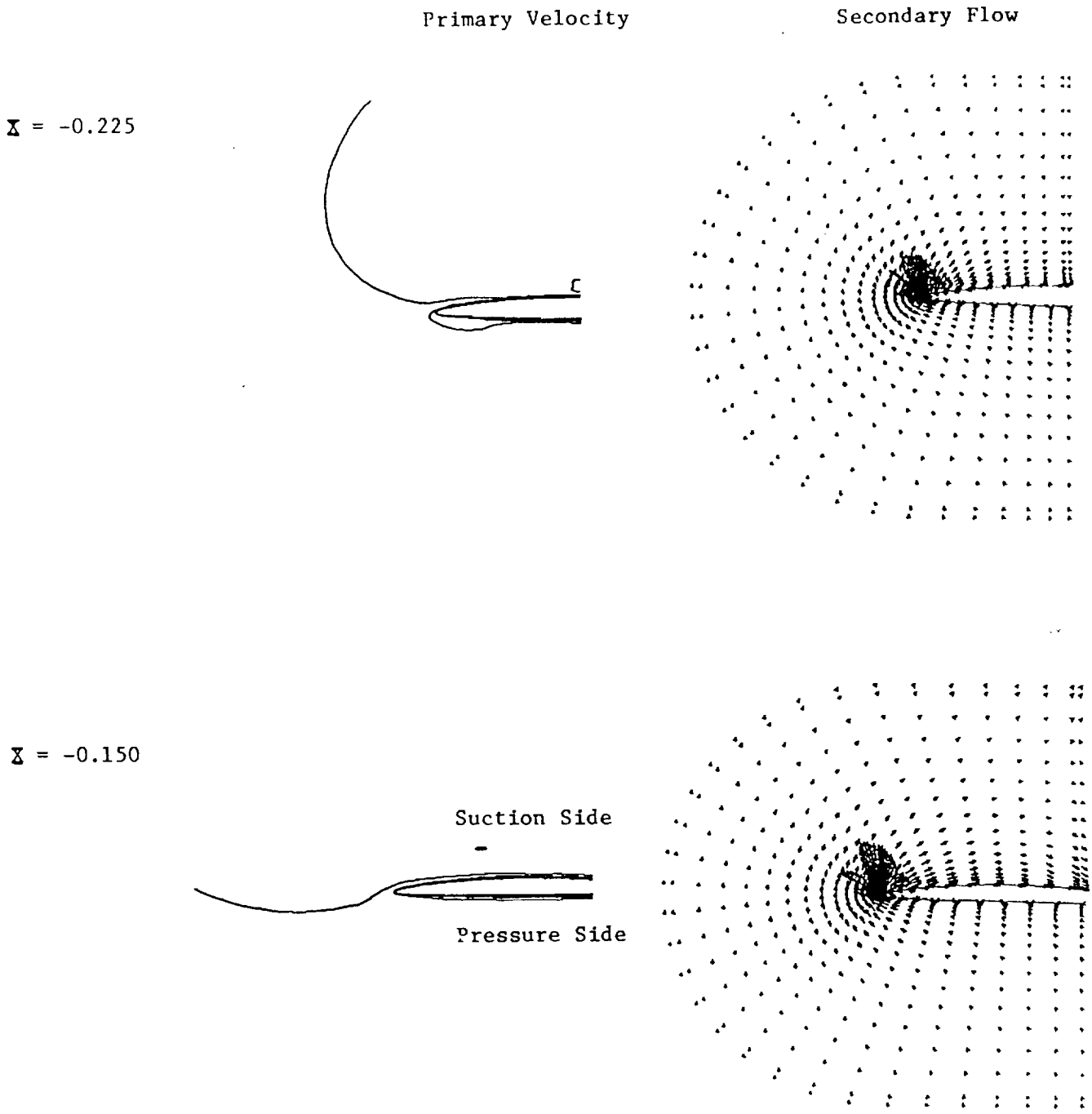

Figure 17a. Tip vortex development in the tip region of a SR3 blade with inviscid flow field. Re = 3×10^5.

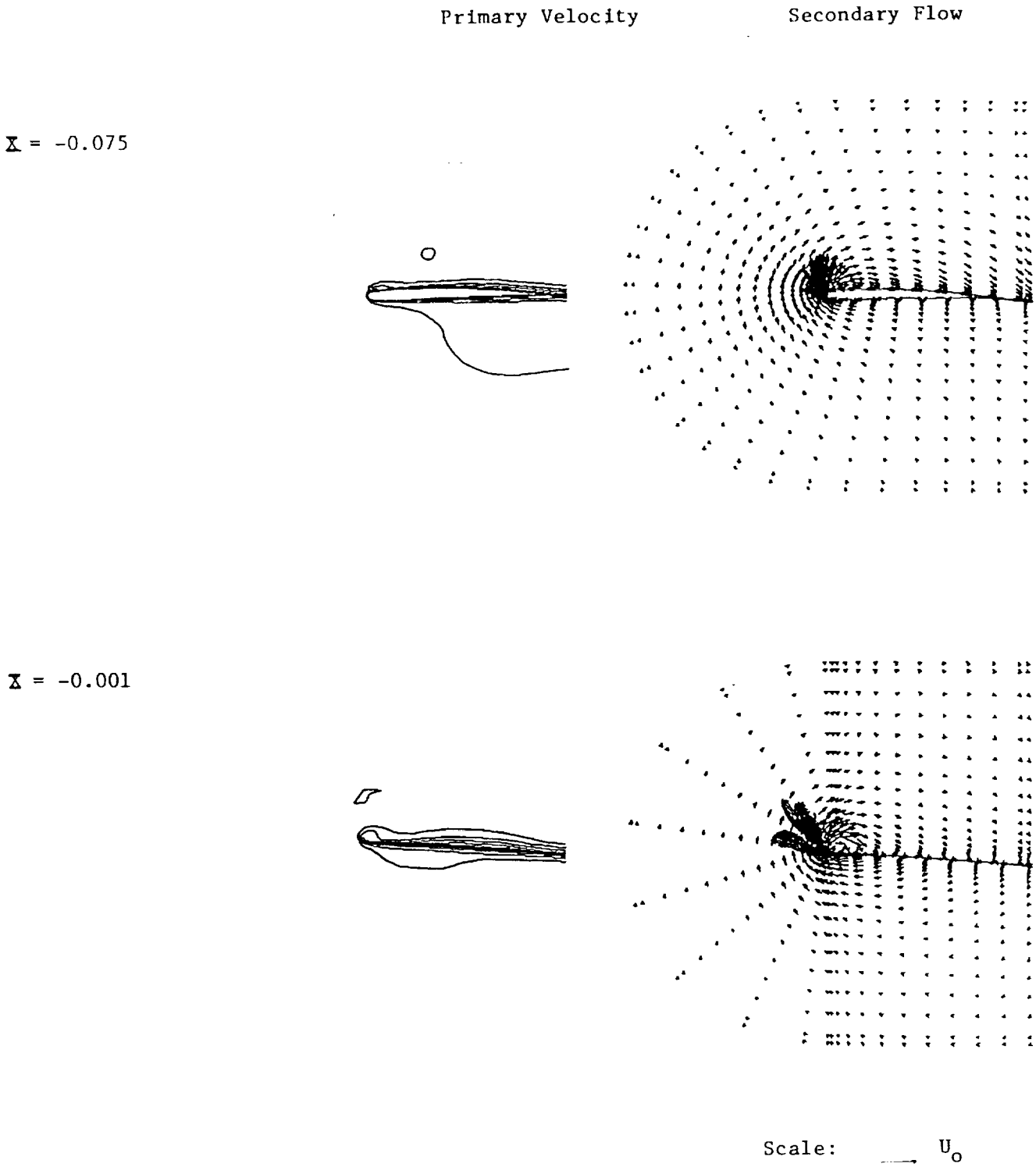

Figure 17b. Tip vortex development in the tip region of a SR3 blade with inviscid flow field. Re = 3×10^5.

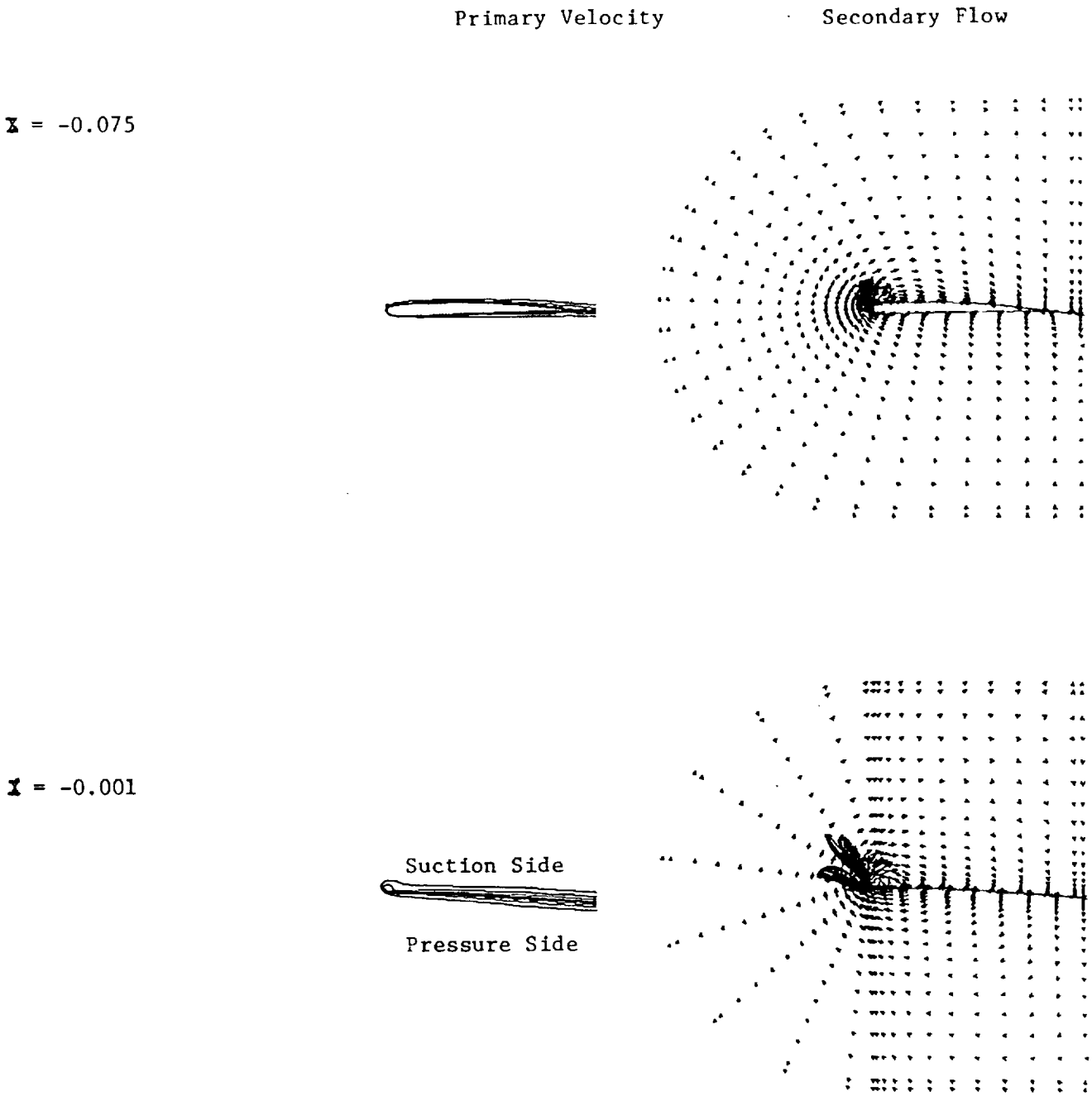

Figure 18. Tip vortex development in the tip region of a SR3 blade without inviscid flow field. Re = 3×10^5.

field possess qualitatively similar characteristics as the calculation with the potential flow field. Finer resolution is suggested for the above turbulent cases, especially near the tip, since the local secondary velocities are very large near the tip for turbulent flow.

An additional series of test cases was performed at a Reynolds number based on propeller diameter of 1.1×10^6. The flow in the tip region accelerates to produce a significantly higher velocity than the freestream. As the freestream Mach number was increased, the local Mach number in the region of the tip also increased. When the freestream Mach number was .35, the Mach number in the vicinity of the tip was approximately 0.8. Higher freestream Mach numbers were tried for turbulent flow; however, local supersonic flow near the tip caused these calculations to abort.

CALCULATIONS DOWNSTREAM OF THE BLADE TRAILING EDGE

The generalization of the PEPSIG/SR3 code to model the tip vortex flow configuration in the region of the trailing edge and downstream wake region represents a new capability. Modifications were made in the grid generation, equations and matrix inversion sections of the PEPSIG code. These modifications enable tip vortex calculations to be continued downstream of the blade trailing edge if the trailing edge is straight and unswept. An attempt was made to extend this capability to swept trailing edges, but further work is required to include this capability in the analysis. An explanation of the modifications to the code and a sample calculation follow.

Special consideration has to be given to the tip vortex flow computation in the region of the trailing edge since the zero thickness of the trailing edge presents a coordinate singularity problem at the rounded part of the tip (see Figs. 19 and 20). By keeping a very small thickness at the trailing edge, the above-mentioned problem can be avoided. Care has to be taken to ensure the smooth variation of the grid space near the rounded part of the tip.

In order to compute the wake downstream of the tip trailing edge, special treatment is provided along the downstream extension of the blade surface since the nonslip boundary condition no longer applies. To avoid the aforementioned coordinate singularity, a small thickness is maintained at the blade trailing edge. Governing equations are written along the two sides of the blade extension. That is, the volume between the blade extensions is now included in the

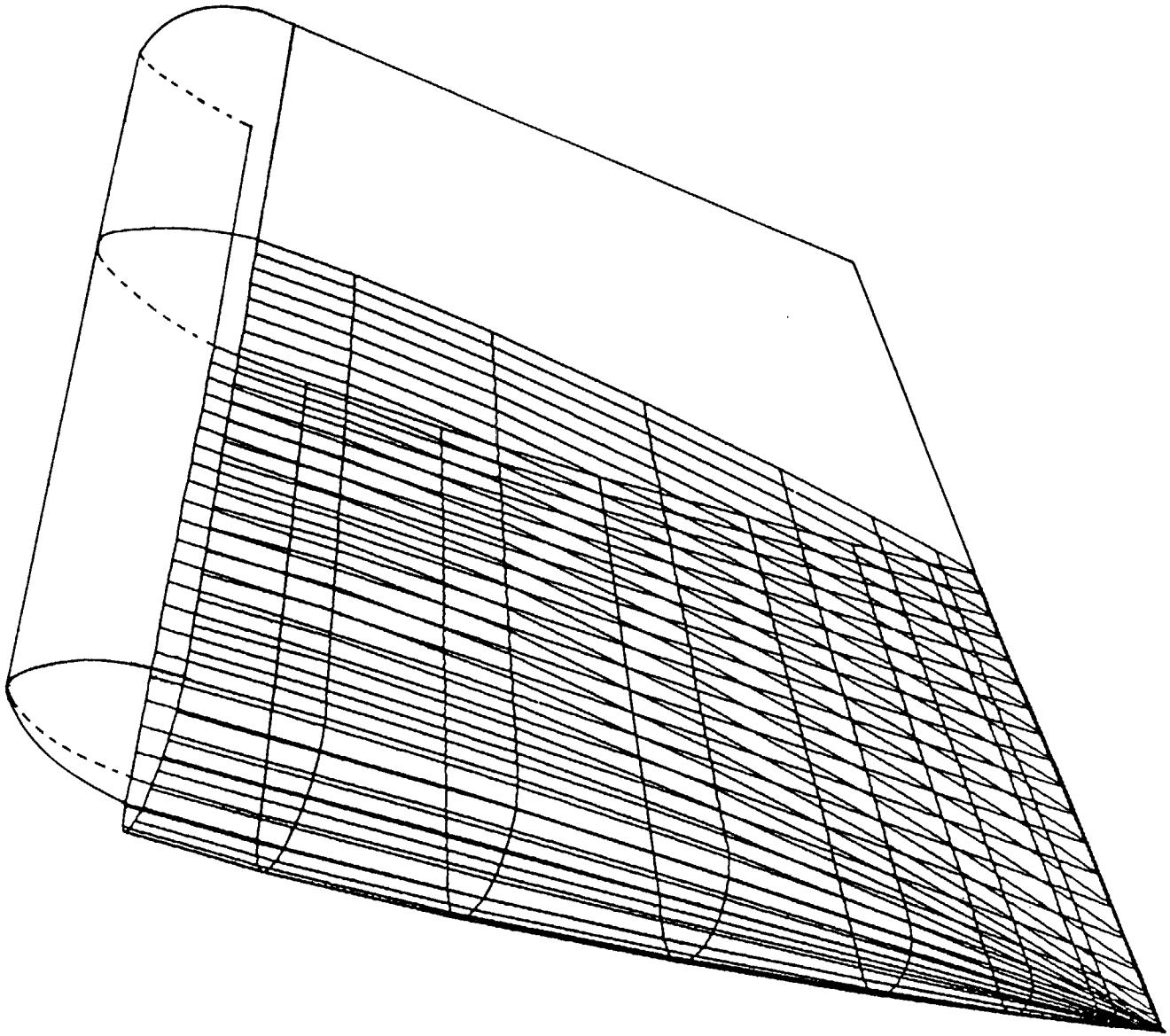

Figure 19. A perspective view of a NACA0012 wing tip.

Σ = 0.20

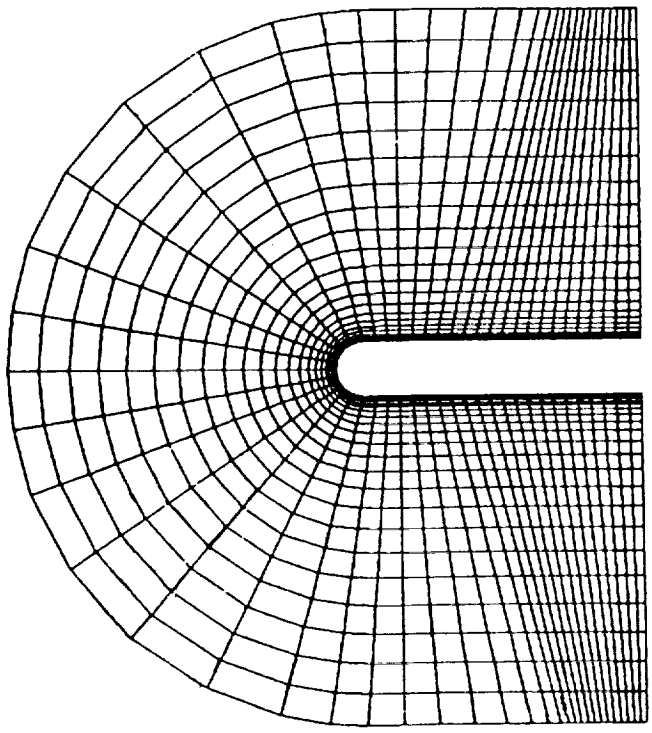

Σ = 1.00

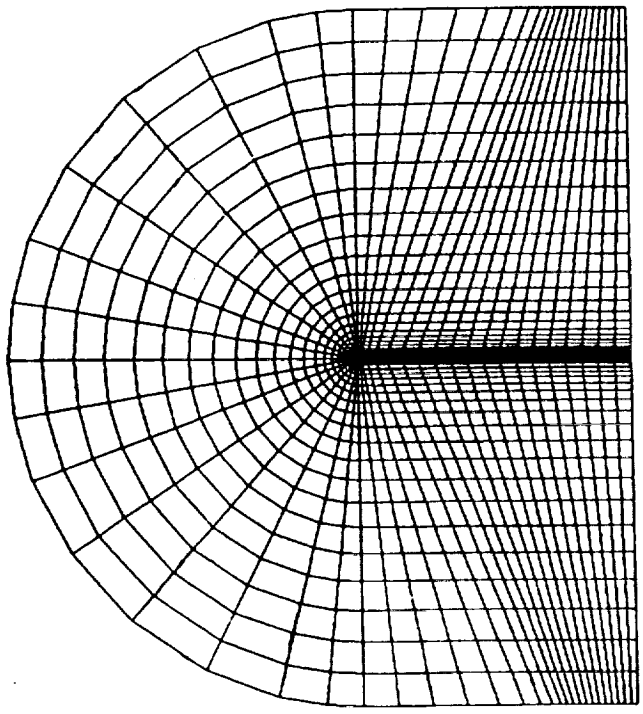

Figure 20. Cross-plane grids and cross-sections of NACA0012 wing tip at the starting station and the trailing edge.

in the computational domain and points on the blade extensions are treated as interior points in the flow calculation. The two ADI solvers (scalar and coupled solvers) were modified for this flow region. At the blade extension boundaries, the boundary conditions were changed to write governing equations for the streamwise momentum equation, scalar potential equation and streamfunction-vorticity.

On the blade, the turbulence model used is the algebraic model presented in the previous section of this report. In the wake region, the modified Bushnell wake model is used for evaluating the turbulent properties. The mixing length is estimated as follows:

$$\ell = 0.07 \min (d_1, d_2)$$

where

$$d_1 = 0.48 (d_o + 0.24x') + 0.15x'$$

$$d_2 = 0.96 (d_o + 0.24x')$$

d_o is an estimate of the wake shear layer thickness at the thickness edge computed from an integral boundary layer calculation and x' is the normal (helical) distance from the trailing edge to the computational plane.

A turbulent flow calculation was performed for the computation of the tip vortex flow field in the region of the trailing edge and downstream of the trailing edge. A NACA0012 wing tip region was used with a round tip (see Fig. 19). The cross-section of the blade tip and the computational grid at the initial station and at the trailing edge station are shown in Fig. 20. Grid points were clustered in the regions of large velocity gradients such as near the blade surface and the tip region.

The Reynolds number based on the tip chord length (the reference length for this series of calculations) C, was 50,000 and the Mach number was 0.24. The angle of attack was 6.2° producing a velocity normal to the blade surface of about 11% of the freestream velocity. The initial boundary layer thickness was 0.01 C.

The calculation was started from about 20% of the chord length, carried downstream to the trailing edge and further into the wake, to a distance 2.14 chords downstream of the blade trailing edge.

Figure 21 shows the development of the tip vortex in terms of the streamwise velocity contours and the secondary flow pattern. The computational results at three streamwise stations (x/C = 0.432, 0.862, and 1.000) were chosen to display

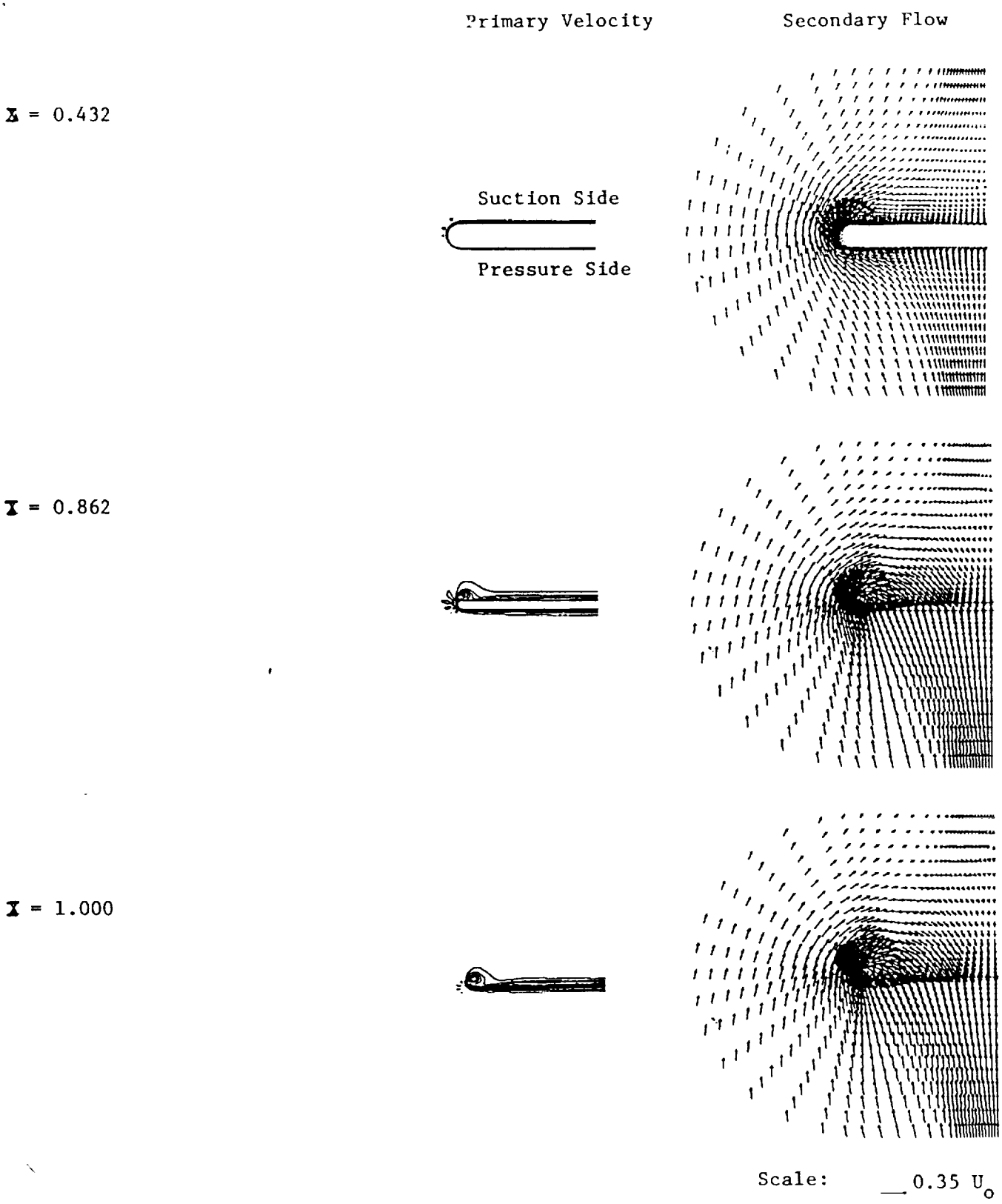

Figure 21. Development of a tip vortex in a NACA0012 wing tip region. Re = 50,000.

the development of the tip vortex on the blade. Note that in these calculations, the leading edge is at x = 0 and the wake is in the region x/c > 1.0. As the flow developed downstream toward the trailing edge the boundary layer on the suction side of the blade became thicker than on the pressure side due to the transport of the low momentum fluid from the pressure side boundary layer around the tip to the suction side. The same flow process was seen in the secondary flow pattern as a transport of vorticity around the tip. The accumulation of the low momentum fluid on the suction side of the tip region as the flow developed towards the trailing edge is characterized by the bulge of the primary velocity contours and the large transverse velocities around the tip. The vortex generation is a result of the secondary flow separation.

The development of the tip vortex into the wake is shown in Fig. 22. The overall picture of the process shows that the magnitude of the secondary flow velocity components which form the vortex persists with little change as the trailing vortex develops downstream.

Three stations in the wake were chosen to display the vortex characteristics of the blade (x/C = 1.005, 1.722, and 3.139). At x/C = 1.005, right after the trailing edge, the blade disappeared and the secondary flow was pushed from the high momentum region towards the low momentum region. As the wake developed further from the trailing edge, the shear layer became thicker and thicker due to diffusion of the wake. The attenuation of the wake can be seen from the thickening of the shear layer and from the increasing of the minimum primary velocity in the wake indicated as nondimensionalized by freestream velocity adjacent to each wake contour plot in Fig. 22. This mechanism also caused the enlargement and weakening of the vortex. At x/C = 3.139, the vortex moved upwards and to the right due to the angle of attack and the transfer of the momentum from high momentum region to the low momentum region.

Since no experimental data for the above cases was known to the authors to validate this study, the comparison was not made. The above analysis was computed without accessing the potential flow by potential flow solver. For non-straight blades, the potential flow may be necessary for estimating the streamwise pressure gradients.

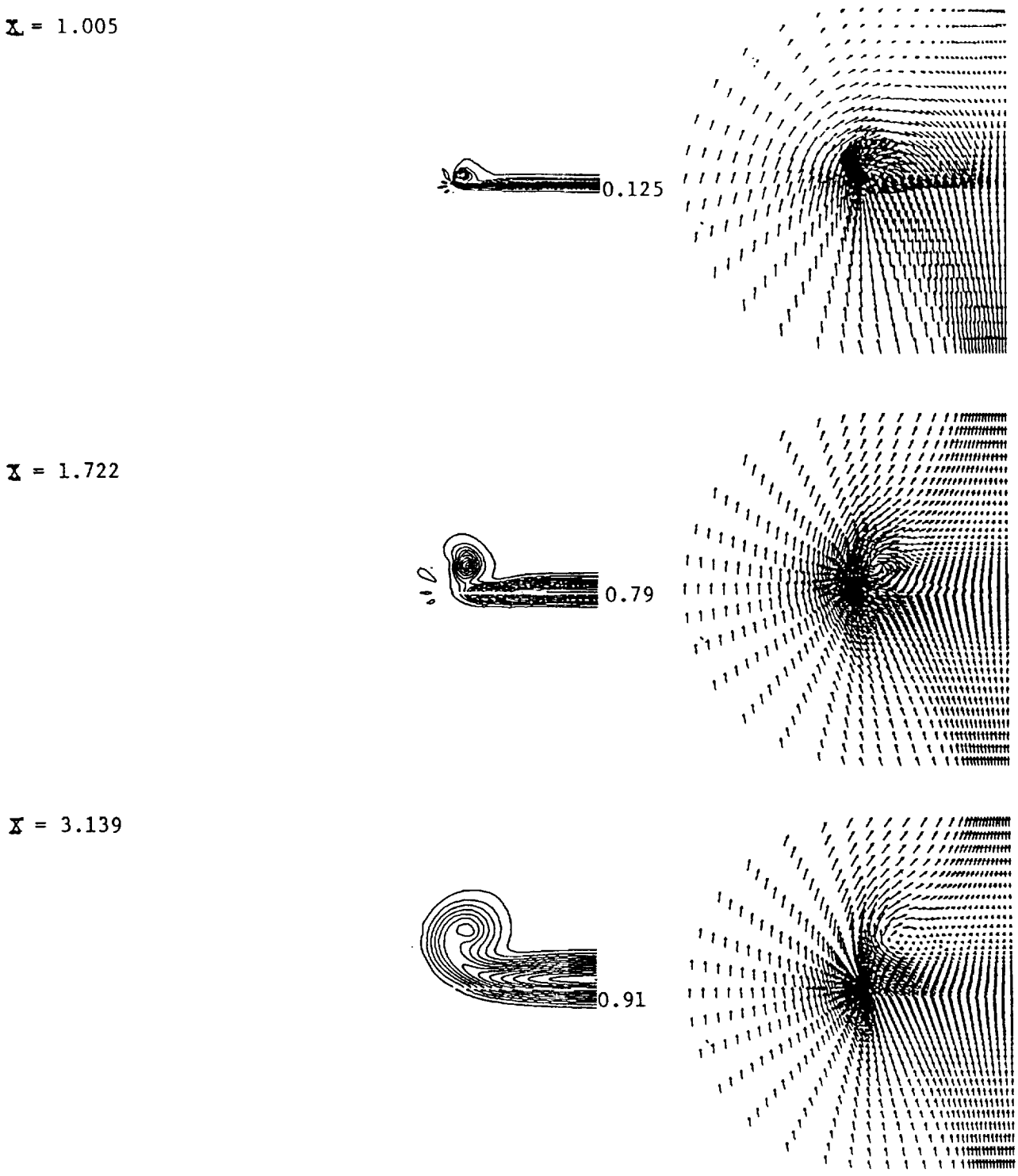

Figure 22. Evolution of a trailing vortex in the wake region downstream of a NACA0012 wing tip. Re = 50,000.

PARAMETRIC STUDY

A parametric study was performed to investigate the effect of blade tip thickness on the strength of the tip vortex. The study was performed on a blade with the SR3 planform operating at an advance ratio, $J = \pi V_\infty / V_{tip} = 3.06$. The Reynolds number based on diameter was 40000 based on propeller diameter and the free stream Mach number was 0.24.

A sequence of calculations was performed at a range of blade tip thicknesses in 2% intervals from 2% thick to 12% thick. The calculations were started at $x/D = -.30$ where D is the diameter of the propeller and x is the tip chord whose origin is placed at the tip trailing edge. The calculations were performed from $x/D = -.30$, which is on the swept leading edge, to $x/D = -.036$ just upstream of the tip trailing edge. Figure 23 shows the secondary flow pattern for the 2% thick blade at $x/D = -.036$. The predominant crossflow is from the left (pressure side) to the right around the blade tip. A tip vortex has formed on the right side of the blade. The vortex center in Fig. 23 is a distance of approximately 10% of tip chord to the right (suction side) of the blade.

Between the blade and the center of the vortex, the flow runs outward along the blade. This outward flow is induced by the vortex and runs counter to the general pattern of clockwise flow around the blade. For the thicker blades studied the qualitative nature of the flow remains the same with the center of the vortex remaining approximately as shown in Fig. 23. However, for the thicker blades studied the maximum magnitude of the outward directed flow between the vortex center and the blade decreases. Since this outward flow is induced by the vortex, the maximum magnitude of this outward flow is used as a measure of vortex intensity. A plot of the magnitude of the vortex induced outward velocity is presented in Fig. 24 as a function of blade thickness. Thinner blades are seen to give more intense vortices. In the range of 8% to 12%, the vortex intensity is seen to be relatively insensitive to blade thickness.

COMPARISON WITH DATA AND DISCUSSION

A test case was run to compare the PEPSIG tip vortex calculation with the F4 propeller data supplied by NASA Lewis Research Center. The data was taken in planes normal to the propeller axis and was provided by NASA in a fixed frame of reference. Under the subject study SRA transformed the data to the rotating

propeller frame with one axis aligned with the blade tip chord and a second axis aligned through the propeller axis of rotation. The third axis was orthogonal to the first two axes.

A calculation of the flow over the F4 blade tip was performed. The calculation was run at an inflow Mach number of .24 and a Reynolds number of 0.6×10^6. The design advance ratio was 2.80. The calculation proceeded from just aft of the tip leading edge to just before the tip trailing edge. The intense tip vortex usually seen in the calculations was not evident in the F4 calculation. The reduced intensity of the tip vortex formation may be due to the blade shape and reduced geometric angle of attack at the tip.

Swirl of the flow is induced by lift of the blade. Computed swirl angles just upstream of the blade trailing edge were compared with measured swirl angles in the first measuring plane downstream of the blade. These swirl angles are compared in the rotating frame. Figure 25 presents a comparison of measured and computed swirl angles approximately 0.1 chord from the suction surface and the pressure surface of the blade. The test data was at axial station #2 (1.99 inches downstream of the stacking axis) and was for the first and last points in the blade-to-blade data tables. The magnitude and shape of the curves are both fairly well predicted, except for the sharpness of the drop in swirl just inboard of the tip.

Figure 23. Secondary Flow Vectors at X/D = -0.036, 2% Thick Blade.

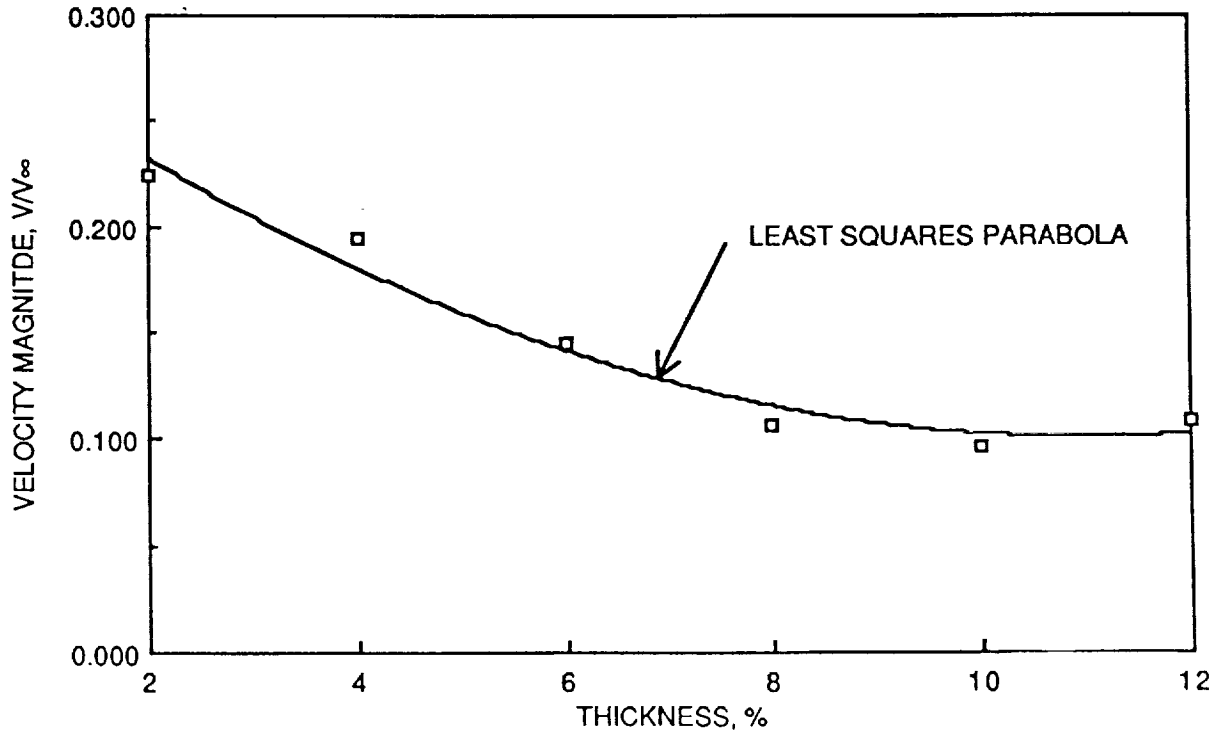

Figure 24. Maximum Velocity Induced by Tip Vortex as a Function of Blade Thickness.

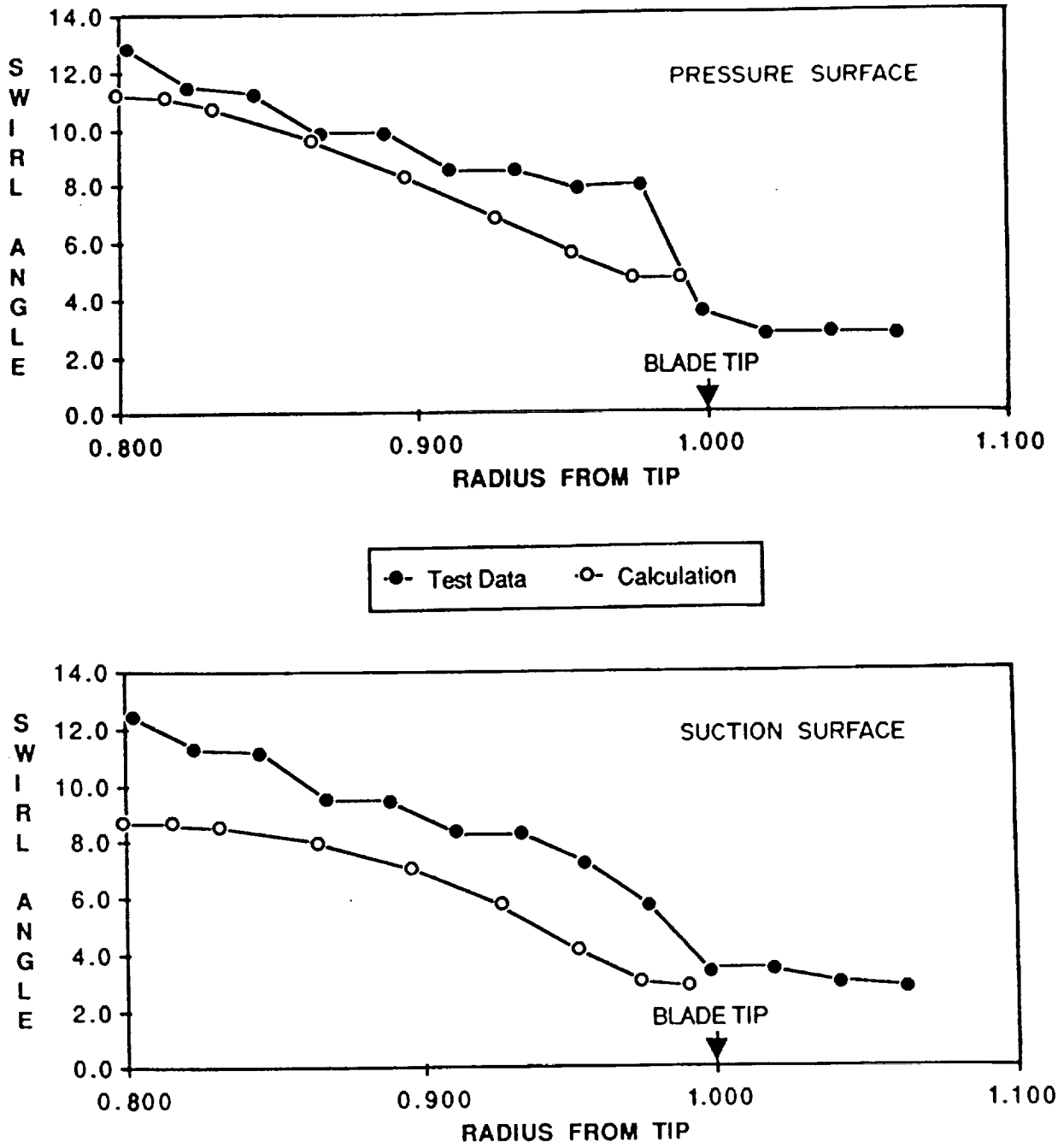

Figure 25. Comparison of Computed and Measured Swirl Angle for F4 Blade.

CONCLUDING REMARKS

A study has been performed to analyze the generation of propeller tip vortices and the resulting flow field for advanced aircraft propellers. A computer code capable of predicting propeller tip flow fields has been developed.

The flow field in the tip region is complex, three-dimensional, and viscous with large secondary velocities. The large secondary velocities preclude the possibility of using conventional boundary layer solution techniques to compute the tip vortex flow. On the other hand, a solution of the full Navier-Stokes equations that adequately resolves the tip vortex flow field would require formidable computational resources. Therefore, an approximate set of three-dimensional viscous flow equations which is applicable to the tip vortex flow field but which does not require the resources needed for the solution of the full Navier-Stokes equations is sought. The parabolic Navier-Stokes equations represent such a set. These equations contain the physical processes of tip vortex generation and can be solved economically by a forward marching procedure.

The subject study accomplished the following tasks:

1. A procedure was developed for inclusion of streamwise pressure gradients into the aircraft propeller analysis. The procedure uses the Hess panel method and interface routine written to interpolate the inviscid pressure gradients onto the viscous grid. Sample calculations using this procedure are presented.

2. The grid generation package was generalized from that used in the Phase I program to allow specification of more general blade shapes and to permit specification grids appropriate for turbulent flow calculations around advanced propeller blades.

3. The generation of a tip vortex on the SR3 advanced aircraft propeller was calculated at a Reynolds number of 1.1×10^6 and included high subsonic Mach numbers of approximately 0.8 in the tip region. A series of both laminar and turbulent flow cases were run showing the tip vortex process on the SR3 blade.

4. The forward marching procedure was extended to compute flow aft of a blade trailing edge. This was demonstrated for a NACA-0012 shaped blade at 6° angle of attack and Reynolds number based on propeller diameter of approximately 10^6. This calculation was used successfully to compute the flow over the blade tip and downstream of the trailing edge including the tip vortex. An attempt was made to extend this technique to blades with swept trailing edges. This extension was unsuccessful and further development is required for these cases.

5. A parametric study was performed to determine the effect of tip thickness on vortex intensity. The blade thickness was varied from 2% of tip chord to 12% of tip chord. The vortex strength decreased with increasing blade thickness.

6. Flow field computations from the forward marching procedure were compared with F4 experimental data provided by NASA. Since most of the data was downstream of the blade, the data comparison could only be qualitative.

7. A Users Manual was prepared.

REFERENCES

1. Briley, W.R. and McDonald, H., "Analysis and Computation of Viscous Subsonic Primary Flows", AIAA Paper 79-1453, 1979.

2. Hess, J.L., "Calculation of Potential Flow about Arbitrary Three-Dimensional Lifting Bodies", Douglas Aircraft Company Report MDC J5679-01, Long Beach, CA, 1972.

3. Kreskovsky, J.P., Briley, W.R. and McDonald, H., "Prediction of Laminar and Turbulent Primary and Secondary Flows in Strongly Curved Ducts", NASA CR-3388, 1981.

4. Levy, R., Briley, W.R., and McDonald, H., "Viscous Primary/Secondary Flow Analysis for Use with Nonorthogonal Coordinate Systems", AIAA Paper 83-0556, 1983.

5. Rohrbach, C., Metzger, F.B., Black, D.M., and Ladden, R.M., "Evaluation of Wind Tunnel Performance Testings of an Advanced 45° Swept Eight-Bladed Propeller at Mach Numbers from 0.45 to 0.85", NASA CR-3505, 1982.

NASA National Aeronautics and Space Administration

Report Documentation Page

1. Report No.	2. Government Accession No.	3. Recipient's Catalog No.
NASA CR-182179		

4. Title and Subtitle
Computation of the Tip Vortex Flowfield for Advanced Aircraft Propellers

5. Report Date
September 1988

6. Performing Organization Code

7. Author(s)
Tommy M. Tsai, Frederick J. de Jong and Ralph Levy

8. Performing Organization Report No.
R88-900064-F

10. Work Unit No.
505-03-01

9. Performing Organization Name and Address
Scientific Research Associates, Inc.
50 Nye Road (P.O. Box 1058)
Glastonbury, CT 06033

11. Contract or Grant No.
NAS3-24881

13. Type of Report and Period Covered
Contractor Report

12. Sponsoring Agency Name and Address
NASA Lewis Research Center
21000 Brookpark Road
Cleveland, OH 44135

14. Sponsoring Agency Code

15. Supplementary Notes
Project Manager,
Christopher J. Miller,
Propeller and Acoustics Technology Branch, NASA Lewis Research Center

16. Abstract

The tip vortex flowfield plays a significant role in the performance of advanced aircraft propellers. The flowfield in the tip region is complex, three-dimensional and viscous with large secondary velocities. An analysis is presented using an approximate set of equations which contains the physics required by the tip vortex flowfield, but which does not require the resources of the full Navier-Stokes equations. A computer code was developed to predict the tip vortex flowfield of advanced aircraft propellers. A grid generation package was developed to allow specification of a variety of advanced aircraft propeller shapes. Calculations of the tip vortex generation on an SR3 type blade at high Reynolds numbers were made using this code and a parametric study was performed to show the effect to tip thickness on tip vortex intensity. In addition, calculations of the tip vortex generation on a NACA 0012 type blade were made, including the flowfield downstream of the blade trailing edge. Comparison of flowfield calculations with experimental data from an F4 blade was made. A User's Manual was also prepared for the computer code (NASA CR-182178).

17. Key Words (Suggested by Author(s))	18. Distribution Statement
Aircraft Propeller Tip Vortex Viscous Flow Three-Dimensional Flow	UNCLASSIFIED - UNLIMITED

19. Security Classif. (of this report)	20. Security Classif. (of this page)	21. No. of pages	22. Price
Unclassified	Unclassified	61	

NASA FORM 1626 OCT 86